

WHAT DINO SAW: ALiBi POSITIONAL ENCODING REDUCES POSITIONAL BIAS IN VISION TRANSFORMERS

PREPRINT - MARCH 18, 2026

Moritz Pawlowsky¹, Antonis Vamvakeros^{2,3}, Alexander Weiss¹, Anja Bielefeld¹,
Samuel J. Cooper^{* 2}, and Ronan Docherty^{2,4}

¹Center for Materials Research, Justus Liebig University, 35392 Giessen

²Dyson School of Design Engineering, Imperial College London, London

³Finden ltd, Building R71, Rutherford Appleton Laboratory, Harwell Science and Innovation Campus

⁴Department of Materials, Imperial College London, London

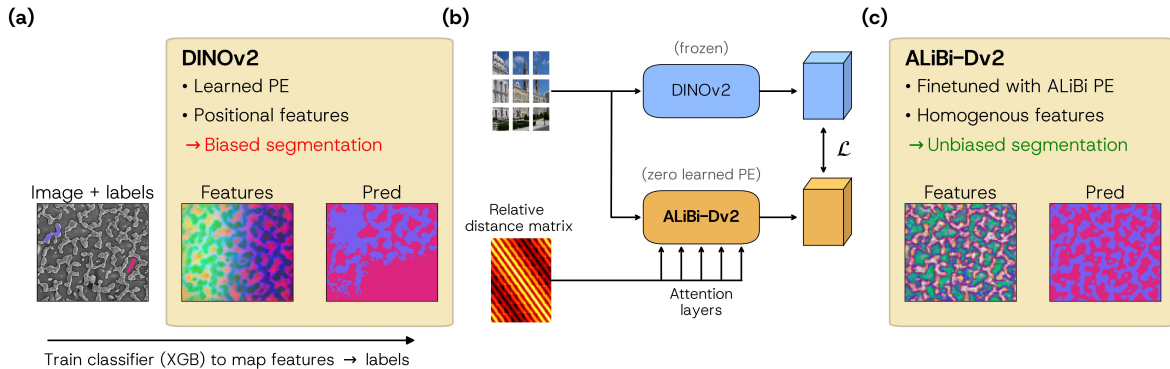


Figure 1: Summary of our contribution. (a) DINOv2’s learned positional encoding (PE) leads to positionally-biased features, which causes poor segmentations when used in zero-shot segmentation of out-of-distribution images. (b) We remove the learned PE of a trained DINOv2 checkpoint, add 2D ALiBi PEs (based on relative token distances at each attention layer) and finetune to target the original embeddings. (c) This produces a model with more homogenous features and better resulting segmentations.

ABSTRACT

Vision transformers (ViTs) - especially feature foundation models like DINOv2 - learn rich representations useful for many downstream tasks. However, architectural choices (such as positional encoding) can lead to these models displaying positional biases and artefacts independent of semantic content. This makes zero-shot adaption difficult in fields like material science, where images are often cross-sections of homogeneous microstructure (i.e. having no preferred direction). In this work, we investigate the positional bias in ViTs via linear probing, finding it present across a range of objectives and positional encodings, and subsequently reduce it by finetuning models to use ALiBi relative positional encoding. We demonstrate that these models retain desirable general semantics and their unbiased features can be used successfully in trainable segmentation of complex microscopy images.

1 Introduction

Vision transformers (ViTs) have become ubiquitous in recent years, with state-of-the-art performance across benchmarks [1], easy multi-modal integration [2] and

strong scalability [3]. Key to this success are the feature foundation models: large backbones, trained via self-supervised learning (SSL) on massive corpuses of images, whose frozen features can be used to train small head networks or in pipelines with no further

*samuel.cooper@imperial.ac.uk

training, such as k -means clustering. Examples include the masked autoencoder (MAE), iBOT and the DINO & JEPA series of models [4–9]; each has different self-supervised objectives and subsequent representations [10], but all display richer and more robust representations than comparable supervised models [11].

The success of feature learning extends across domains - various foundation models exist for (bio)medical imaging, satellite data or robot manipulation - as well as across tasks, existing as backbones inside task-specific foundations models such as SAM [12] and EVA-CLIP [13]. Most of these models (regardless of training objective) use the standard ViT architecture: a patch projection, positional encoding (PE) and some number of attention layers.

Architectural choices clearly influence output feature quality: background attention sinks necessitated the addition of register tokens [14], whilst others have suggested the learned positional encoding is responsible for pernicious ‘feature artefacts’ and trained denoisers to remove them [15]. Contemporaneous work has analysed the flow of information through these models, specifically in terms of the preservation and interaction of positional information with semantic information [16, 17]. The quality and consistency of these ViT features is important for pipelines which use them without additional training, like LOST & MOST’s unsupervised object detection [18–20], various (spectral) clustering methods for semantic segmentation [21–23], and user-guided ‘trainable segmentation’ of images [24–27].

The application of computer vision to materials science imaging suffers from several challenges: scarcity of open data, a wide range of length scales and materials systems, and the ambiguities of electron microscopy [28]. This makes the general, ‘off-the-shelf’ features of foundation models appealing (especially in low- or no-training pipelines), and several works have leveraged them successfully [26, 29]. However, materials science images, typically captured with a Scanning or Transmission Electron Microscope (SEM/TEM), are fundamentally different to natural images: they are grayscale, are sometimes hundreds of megapixels large, and are often homogeneous cross-sections. This homogeneity is especially challenging given the clear positional biases seen in ViTs like DINOv2, which has been shown to have negative impacts on trainable segmentation [26].

In this work, we seek to reconcile these differences by finetuning a ViT (*i.e.* DINOv2) with 2D-aware ALiBi positional encoding [30]. First, we characterise the positional bias across various literature ViTs using linear probes, finding some channels of the output features

which are almost purely positional ramp functions regardless of input image. These exist in both MAE and DINO models, and across different positional encodings (learned or RoPE), though not in supervised ViTs.

Next, we finetune DINOv2 checkpoints to use 2D-aware ALiBi positional encodings, with cylindrical boundary conditions and normalisation to enable positional encoding interpolation [31]. Surprisingly, once the learned PE is replaced with the unbiased ALiBi PE it is sufficient to use the (biased) embeddings of the original DINOv2 model as a training target to recover semantics.

Finally, we benchmark the performance of this finetuned ALiBi-DINOv2 (ALiBi-Dv2) in terms of both its homogeneity and linear-probe performance on standard segmentation benchmarks (VOC, ADE20K), finding that performance is largely maintained and even improved in some cases. We further apply our ALiBi-Dv2 to weakly- or unsupervised tasks (k -means clustering and trainable segmentation) and find that its homogeneous features improve the resulting segmentations.

2 Background

2.1 Vision Transformers

Transformers are artificial neural networks which process a series of ‘tokens’ (projections of discretisations of some input sequence $T = \{\mathbf{t}_1, \mathbf{t}_2, \dots, \mathbf{t}_N\}$) which learn to update the representation of some d dimensional token \mathbf{t}_i with respect to all other tokens via attention,

$$\text{Attn}(\mathbf{Q}, \mathbf{K}, \mathbf{V}) = \text{softmax}\left(\frac{\mathbf{Q}\mathbf{K}^\top}{\sqrt{d}}\right)\mathbf{V} \quad (1)$$

where $\mathbf{Q}, \mathbf{K}, \mathbf{V}$ are packed matrices of the query, key and value learned projections of T [32, 33].

Vision transformers discretize an input image into $s \times s$ px non-overlapping patches and perform a learned linear projection to map from $\mathbb{R}^{B \times C \times H \times W} \rightarrow \mathbb{R}^{B \times d \times N_t}$ where $N_t = \text{number of tokens} = HW/s^2$ [34]. This is done to avoid the overhead of processing HW pixels via the n^2 attention mechanism.

The patch projection followed by multiple attention layers is common across most ViTs. ViTs tend to have a ‘size’: (S)mall, (B)ase, (L)arge *etc.*, which have corresponding hidden dimension d of 384, 768, 1024 *etc.*, as well as having a greater MLP dimension and more attention heads.

2.2 Positional encodings

Attention is fundamentally unordered, so transformer models attach a ‘positional encoding’ in order to associate each token with its position in a sequence [32]. Typically these are injected (*i.e.* added to the patch’s linear projection) at the start of the model, and the model then learns to use them alongside token content across the layers of the network.

Early work with vision transformers experimented with simple positional encodings, such as raster-scan order (an increasing integer index from left-to-right, top-to-bottom), sinusoidal (adding sinusoids of increasing wavelength along the channel dimension) and learnable 1D encodings [34, 35]. These are absolute positional encodings: they uniquely identify each token with a given position in the original image. Note that sinusoidal encodings can theoretically uniquely identify tokens in a sequence up to the largest wavelength added.

Different encodings, such as 2D-learned, relative positional encodings or no positional encoding (NoPE), were tried, but did not improve benchmark performance and so were not used [34]. To generalise to new image sizes, the positional encoding can be interpolated with respect to the new sequence length.

2.3 Relative positional encodings and ALiBi

Relative positional encodings (RPE) encode position information in terms of relative distances between two tokens. This can be additional relative attention, where the query content attends to relative positional keys [34], or in the recently popular Rotary Positional Encodings (RoPE) [36] a rotation of query-key dimension pairs proportional to token positions, such that only relative position are expressed inside the attention inner product. Similar to sinusoidal encodings, the rotation applied to dimension pair d of a token t decreases as d increases.

Attention with Linear Biases (ALiBi) introduced positional encodings as linear offsets added to token-token attention scores as a function of their relative distance [30]. Concretely, the ALiBi attention scores for the i th query \mathbf{q}_i are

$$\text{softmax}(\mathbf{q}_i \mathbf{K}^\top + m \cdot [-(i-1), \dots, -2, -1, 0]), \quad (2)$$

where m is a head-specific scalar, which can be learned or set according to a fixed geometric progression [30]. This encourages different heads to focus on different distances. ALiBi enforces ‘an inductive bias towards recency’ (for images, proximity) and operates directly on attention scores, rather than encoding information in a token’s hidden state [30]. ALiBi positional encodings

can also benefit from the ‘interpolation trick’ in order to improve length generalization [31].

A few ViTs have integrated relative positional encodings: MViTv2 uses decomposed RPEs [37], DINOv3 uses a modified RoPE variant [8] and domain-specific models like CROMA (in satellite imaging) [38] and Long-MIL (for histopathology imaging) [39] have used 2D-aware ALiBi PEs. This choice of RPE improved various properties such as shift-equivariance and length generalization.

2.4 DINO & feature learning

The scalability of transformers and of SSL led to the development of large, general-purpose ‘feature foundation models’. One of the earliest examples is DINO (self distillation with no labels), which showed that self-supervised vision transformers learnt meaningful decompositions of images in a way that similar convolutional neural networks did not [6].

DINOv2 repeated the approach on a large curated dataset, producing ‘all-purpose visual features’ that enabled state-of-the-art performance on benchmarks with linear probes [7]. DINOv3 applied various tricks (such as Gram anchoring) to produce dense, coherent feature maps for high-resolution images [8]. Both DINO and DINOv2 used learned 1D positional encodings, whereas DINOv3 used RoPE positional encoding, ostensibly to avoid positional leakage into the features [8, 40].

2.5 Feature artefacts & positional bias in ViTs

Despite their impressive performance on benchmarks, the DINO features (and ViT features more broadly) exhibit certain biases and artefacts. The authors of ref. [14] found anomalous high-norm background tokens caused by the model’s re-use of them for computation. They ameliorated this by adding scratchpad ‘register tokens’ ([REG]) which were discarded at the end of the forward pass.

‘Denosing vision transformers’ (DVT) [15] noted that feature artefacts were largely independent of semantic content and were correlated with the featuremap of the zero-input tensor, and suggested a link between the positional encoding and these artefacts as a possible explanation. Weak artefacts were noted even in a DINOv2 checkpoint with [REG] tokens. They trained an additional denoiser network to remove these artefacts. We noted these denoised feature map PCAs also appeared to display less left-to-right positional gradients, and therefore included them as a comparison in Sec. 4.

Recent work has examined the role of positional information in feature representation in ViTs. One study demonstrated that tokens were locally connected even after projection into a lower-dimensional non-positional basis as evidence for a ‘linear representation hypothesis’ of ViT features [16]. Another study examined the role of position and content interactions inside ViTs, pointing to ‘low-energy’ positional modes inside the features which diminish in importance through subsequent layers of the network [17]. They further showed how the positional structure of DINOv2 was preserved as a 2D sheet across layers, whereas supervised ViTs collapsed this information into a ‘quasi-1D structure’.

2.6 Trainable segmentation

Trainable segmentation (also called ‘interactive segmentation’ or ‘pixel classification’) is a weakly supervised segmentation technique that trains a classifier to map from a set of features describing pixels to user-drawn labels [41, 42]. Popular implementations use a classical multi-scale feature set (Gaussian blurs, Sobel or Laplacian edge detection, Hessian filters *etc.*) and a lightweight fast classifier like a random forest (capable of modelling non-linear interactions) [41, 42]. Once trained, the classifier can be applied to unlabelled pixels to produce a segmentation.

Trainable segmentation tools are often used in bio-image segmentation [41–44], and occasionally applied in materials science imaging [45–47]. One drawback of the approach was the relative inexpressiveness of the classical features when applied to more complex features [26], such as crack networks, imaging artefacts (beam damage, charging, curtaining in electron microscopy data) or the ‘pore-back’ effect [47] in porous media.

Several works aimed to fix this problem by combining the classical and ‘deep’ features of ViTs and CNNs in a trainable segmentation workflow, which produced better segmentations of complex microscopy images [24–27]. However, some noted the difficulties presented by the positional biases of ViTs, especially in the materials science context where researchers frequently image large cross-sections of homogenous materials [26]. Attempts to reduce these positional biases by averaging over transformations (flips, rotations) were moderately successful but failed to reduce centrosymmetric biases and came with associated runtime costs [26].

On the nano- and micro- length scale, these materials are effectively semi-infinite random arrangements of microstructural features, often with no central focus or preferred direction - a classifier fit to positional informa-

tion inside the features is therefore often wrong. There is, in essence, a mismatch between the architectural biases and training data of the models, and the images researchers wish to analyse.

3 Method

3.1 Positional linear probing

One simple way to analyse positional biases in ViTs is via linear probing of output features. If positional information is linearly present in combination (or worse, in isolation) in the output feature channels, then any secondary classifier (linear/logistic regressor, random forest, XGBoost, *etc.*) can fit to it.

We trained linear probes to map from both the full feature stack and single channels of output and layer-wise ViT features to a series of 1D ramp functions: left-right, up-down, diagonal and radial. Ramp values were normalised from 0-1 across the image. Probes were fit over a randomly sampled subset of spatial patches, and R^2 was measured over holdout regions. In practice, around 2.5% of patches were sampled to train the probe. The ramps and example samplings can be seen in Fig. 2.

Values were averaged over a dataset of 15 microscopy images (micrographs), examples of which are available in Sec. S1.1. We tested the same linear probing setup on two additional datasets: 60 random textures (of everyday objects) from the ‘Describable Textures Dataset’ (DTD) [49] and 60 instances of uniform white noise. 10 repeat measurements (with different samplings) were made for each image.

Spatialised subsampling was tested (*i.e.* with holdout vertical and horizontal regions) but did not make a significant impact, neither did choice of regularised (Ridge) or unregularised regressor.

To produce a single numerical positional bias ‘score’, multivariate linear regression was performed to jointly predict the normalised (x, y) coordinates from the full feature stack.

3.2 ALiBi DINOv2

Being injected at the very start of the network means positional encodings are integral to the learned representations of ViTs. We experimented with schemes to adapt the existing learned positional encoding to make it more homogeneous (tiling, zooming, *etc.*) but were unsuccessful: either output features were degraded or still displayed edge effects. This motivated some form of further training with a positional encoding that was homogeneous by construction.

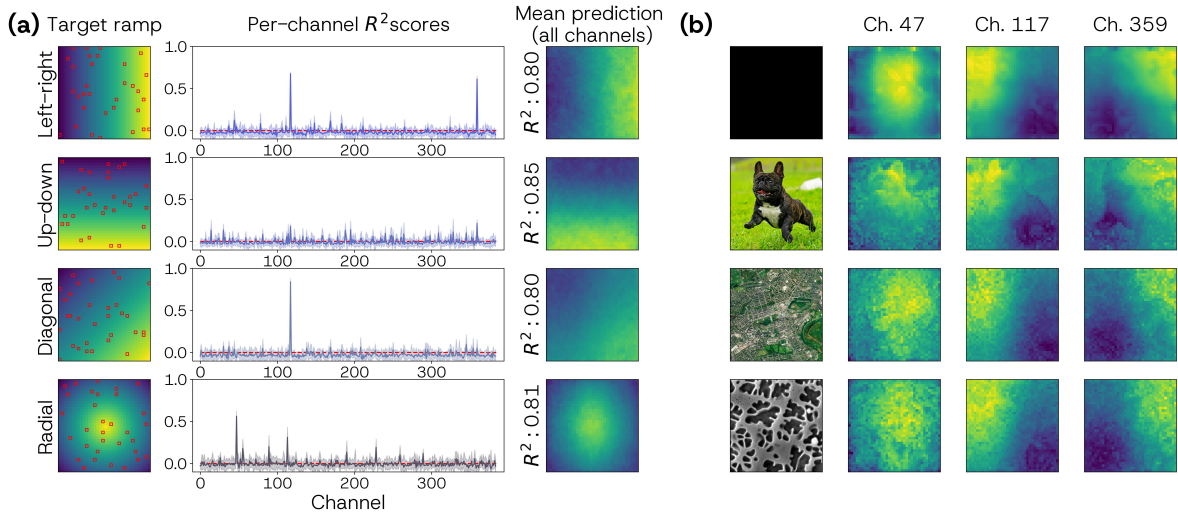


Figure 2: Linear probe analysis of DINOv2-S features. **(a)** We train linear probes to map from image features (or individual channels) to randomly sampled (red squares) ramp functions, reporting R^2 scores on holdout regions. Per-channel scores and predictions (which use all channels) are both averaged over a dataset of 15 homogenous microscopy images, *i.e.* images with no preferred direction. **(b)** The channels with the highest positional R^2 scores for a series of images, including a satellite image and an electron microscope image of a nickel superalloy [48].

We found RoPE models could still express positional bias (see Sec. 4.1 and Tab. 1), and therefore elected to use ALiBi encodings. We used Euclidean distance as the distance metric with wrap boundary conditions in order to avoid asymmetries in the distance matrix. We used a fixed $m = 1$ for all head-specific scalars to avoid potential asymmetries compounding across layers (we examine the impact of trainable heads in Sec. S2.2). ALiBi offsets were added to each attention layer. The entries in the ALiBi distance matrix were normalised between 0-1 by dividing by the longest distance. The learned PE was frozen and set to zero during finetuning.

In terms of training target, we found it was sufficient to use the embeddings of the original (biased) DINOv2 as a teacher. Our motivation was as follows: those embeddings had many of the desirable general semantics we wished to preserve, they were simple and cheap to generate, and the setup of our ALiBi PE made it difficult for our model to express those biases, even when present in the data. We experimented with producing ‘cleaned’ target embeddings by directly averaging over the features of transformations of the input images, but these were costly to produce and did not improve performance. During training, we zeroed the four most positional channels as identified in Sec. 4.1.

The dataset used to generate embeddings was COCO-Stuff [50]. Images were sampled with shortest-side resizing to 224 px followed by a center crop to (224, 224) px. No training augmentations were used, though these could be added in future to improve properties, such as rotation equivariance. Following DINOv2, we

performed a short period of multiscale training at (518, 518) px resolution [7]. We found this was important to improve length generalisation of the model - see Sec. S2.3 for more details.

Further training details (learning rates, batch size, *etc.*) are available in Sec. S2.1. As a baseline comparison for the benefits of ALiBi encoding, we also finetuned a DINOv2 checkpoint with no positional encoding (*i.e.* a bag of patches). We refer to this model as ‘NoPE’ in the following sections. The training setup for ALiBi-Dv2 and NoPE was identical.

4 Results and discussion

In this section we characterise the positional biases across literature ViTs via linear probing, and how this motivates the training of a homogeneous feature model (ALiBi-Dv2). We proceed to examine the properties of our ALiBi-Dv2 in terms of feature PCAs, linear probe semantic segmentation (VOC, ADE20K) and weakly-supervised segmentation of materials microscopy images.

Unless otherwise stated, we used DINOv2-ViT-S (patch size 14) with [REG] tokens as ‘DINOv2’, DINOv3-ViT-S+ (patch size 16) as ‘DINOv3’ and DINOv2-ViT-S + [REG] + Denoising Vision Transformer’s general lightweight denoiser layer as ‘DVT’.

Model	d	PE	Supervised	R^2_{micro}	R^2_{texture}	R^2_{noise}
DINO	S	Learned	×	0.57	0.53	0.53
	B	Learned	×	0.64	0.59	0.54
DINOv2	S	Learned	×	0.83	0.71	0.89
	B	Learned	×	0.69	0.58	0.89
DINOv3	S+	RoPE	×	0.97	0.90	0.98
ViT (MAE)	B	Learned	×	0.71	0.61	0.71
SAM	256	Learned	✓	0.61	0.66	0.91
ViT (IN1k)	B	Learned	✓	-0.02	0.04	-0.01
DEiT	B	Learned	✓	0.09	0.13	0.04
CLIP	B	Learned	✓	0.11	0.07	-0.04
EVA02	B	RoPE	✓	0.02	-0.18	-0.08

Table 1: (x, y) linear probe R^2 scores for a set of existing models which produce patch-level features. Supervised models - including those with an SSL backbone - have lower R^2 scores. Scores are reported per-dataset: ‘micro’ for micrographs, ‘texture’ for DTD [49] texture images and ‘noise’ for random noise.

Model	d	PE	R^2_{micro}	R^2_{texture}	R^2_{noise}
DINOv2	S	Learned	0.83	0.71	0.89
	B	Learned	0.68	0.58	0.89
DINOv2 (CB)	S	Learned	0.78	0.67	0.89
DVT	S	Learned	0.75	0.68	0.83
ALiBi-Dv2	S	ALiBi	-0.23	0.32	-0.85

Table 2: (x, y) linear probe R^2 scores for DINOv2 variations. ‘CB’ refers to zeroing the 4 most positional channels of DINOv2 (see Fig. 2). Our ALiBi model has more homogeneous features and therefore has a lower R^2 .

4.1 Positional linear probing

Given that positional biases had been observed in DINOv2, we started by performing linear probing on its output features for a series of ramp functions, plotting the result in Fig. 2. The results were averaged over a dataset of theoretically homogeneous microscopy images: this was to avoid true horizontal or vertical gradients (*i.e.* sunsets, the sky, field-of-view) skewing the results.

Of note are the distinct peaks in the per-channel R^2 scores, indicating that some channels were highly correlated with the different 1D ramps. We display these specific channels across a set of different images and see that the output features are consistently positional (radial or diagonal gradients) regardless of image content. When predicting using all channels of the feature stack, the resulting R^2 is high, *i.e.* consistently 0.8 or above.

To identify how widespread the problem was, we then measured the positional bias of a series of literature ViT models via linear probing, presenting the results in Tab. 1. As noted in Sec. 3.1, we regressed onto the (x, y) 2D ramp function to produce a single R^2 value that captured both left-to-right and up-to-down biases.

We found biases across all models in the DINO series, including DINOv3, which used a relative positional encoding (RoPE). We also observed biases in a ViT trained with masked autoencoding [4]. Other supervised models like DEiT [52], CLIP [2] and EVA02 [53] were found to have much lower positional bias, and absence of problematic positional channels. This supports Ref. [17]’s claim that self-supervised models preserve positional information more strongly than supervised models.

The relatively high positional score of the SAM backbone complicates the picture: the backbone was initially pretrained with SSL as an MAE ViT, but was further trained in a supervised manner alongside the decoder head to perform promptable segmentation. It is unclear if this high positionality is a holdover from the SSL pretraining, or the fact that it was supervised to perform a dense task (segmentation) compared to the other supervised models, which performed more global tasks (classification or captioning).

When repeating the probes on the DTD we found the R^2 scores to be around 0.05-0.1 points lower for most models, though the trends remained the same (including the same outlier channels). The random noise ramps had a similar set of R^2 scores to the micrograph dataset - the biases appear to be stronger (or less mixed with genuine semantics) in out-of-distribution data.

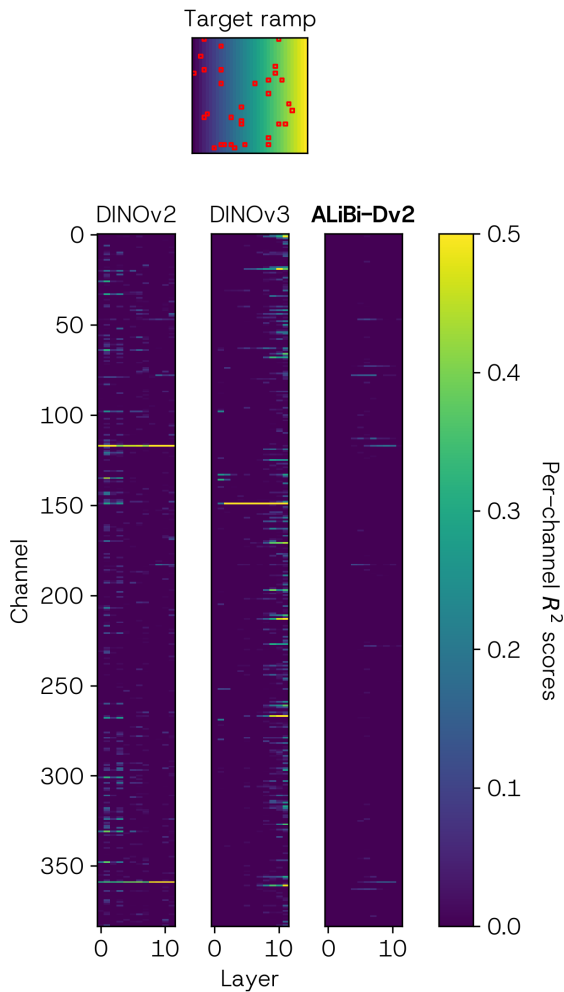


Figure 3: Per-channel per-layer ‘positional fingerprint’ of R^2 scores for DINOv2, DINOv3 and ALiBi-Dv2 for a left-right target ramp. DINOv2 begins with positional information spread across channels (its learned PE is added at the start of the network), which later decreases, whereas for DINOv3 the channels become more positional with layer depth (RoPE is applied at each layer). ALiBi-Dv2 has less positional information present across its channels and layers.

DINOv3’s high positional score was surprising, given the series of adjustments made to the positional encoding (axial RoPE, positional jitter) to improve length generalization and reduce positional leakage [8, 40]. To try and understand why this was the case, we performed a left-to-right linear probe per-channel at each layer of DINOv2 and DINOv3 (again averaged across 15 images), and plotted the results in Fig. 3.

We found DINOv2 began with positional correlations spread across multiple channels, which diminished in the later layers of the network, whereas DINOv3’s positional correlations increased throughout the layers. This can be explained by the structure of their PEs: DINOv2’s learned PEs are injected once at the start,

and DINOv3’s RoPE is applied at each layer. Both models had a small number of highly positional outlier channels.

That DINOv2 loses some positional information throughout its layers has been noted previously by Ref. [17], who trained linear probes to predict exact token position and found the accuracy decreased throughout the network. Whilst our findings in Fig. 3 do support this, we also find that the DINOv2’s R^2 when using all channels remains relatively consistent across layers: the model is able to express these biases even if it loses token-perfect information. We present additional layer-channel plots in Fig. S6. Further works examining how these positional biases arise during training, especially across different objectives and positional encodings, is an interesting avenue of future research.

Next, we compared approaches for reducing the positional bias of DINOv2 and the results are presented in Tab. 2. The approaches were ‘channel-blanking’ (CB), where the four most positional channels of DINOv2 were set to 0 on forward pass, and DVT, the learned denoiser layer. Both reduced (but did not eliminate) the positional bias. We found DVT reduced left-to-right biases but emphasised up-to-down biases.

The failure of these approaches to eliminate the positional bias motivated the training of ALiBi-Dv2 as described in Sec. 3.2. We report the linear probe results for our ALiBi model in Fig. 3 and Fig. S5, as well as Tab. 2. We find greatly reduced positional bias scores across all channels and layers of the network. Additional positional probe plots for different ViTs are available in Sec. S1.4.

4.2 Qualitative feature PCAs

Fig. 4 shows feature PCA visualisations for a series of images. Visualisations were produced by projecting output patch features from $d = 384 \rightarrow d' = 3$ and plotting the 3 components as RGB channels as per DINOv2 [7]. PCAs are fit per-image; images are resized to (518, 518) resolution.

From these PCAs we can observe reduced positional gradients (both left-right and up-down) for ALiBi-Dv2 compared to DINOv2 and DVT. For the synthetic ‘square-circle’ example the resulting features are sharper and more separated, whereas for DINOv2 and DVT, albeit to a lesser extent, the square and circle features appear closer, either due to the influence of the positional encoding or weak artefacts. For some images, such as the dog, the PCAs of DVT and ALiBi-DV2 are similar; this was more often seen in in-distribution

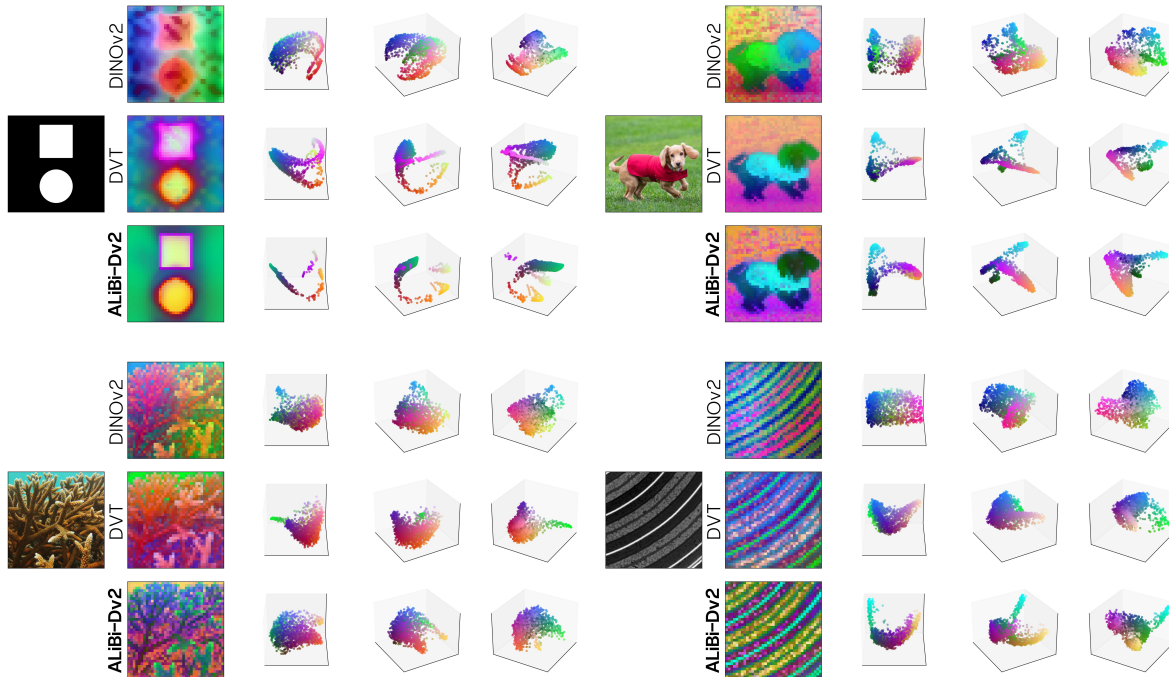


Figure 4: Feature PCA comparisons for DINOv2-S, DVT and our ALiBi-Dv2. ALiBi-Dv2 produces features which are semantically rich but that display less positional bias and artefacts. The token geometry is (locally) smooth, and in many cases similar to that of DVT. Of note is the ‘square-circle’ image, which retains ‘objectness’ across indistinguishable interior patches, the preserved vertical bias of the dog image (from depth-of-field) and the reduced positional biases on the X-ray CT cross-section of a pintype Li-ion battery [51].

images, where the positional bias was expressed less strongly (in relative terms) to the semantic content.

The ‘token geometry’ (3D plot of patch features according using PCA coordinates) remains locally smooth echoing the results of Ref. [16] when projecting DINOv2 features into a learned positional subspace.

Fig. 5 shows further PCA visualisations on larger rectangular images, this time for DINOv2, DINOv3 and our ALiBi-Dv2. Again we see positional biases displayed in the features (some edge effects for DINOv2, ramps for DINOv3), which become more problematic the less ‘natural’ the images become (*i.e.* dogs vs satellite photography vs electron microscopy). Agreeing with the results of Sec. 4.1, we see that DINOv3 appears more positional than DINOv2.

Once again we note that ALiBi-Dv2 retains the ability to decompose large central objects, like the dogs’ heads and bodies, whilst retaining a high degree of homogeneity on more homogeneous images. The ‘bi-modal cathode’ is a scanning electron microscope image of a lithium-ion battery cathode with a mix of different particle sizes - these have better packing and therefore promise higher energy densities. Analysing them is therefore of great interest, and the ALiBi-Dv2 model produces homogenous features of complicated

microstructural concepts such as particle size, cracking and gaps (pores) in the structure.

We note that PCA visualisations are imperfect tools: a feature having less variance and therefore not being present in the first 3 components does not imply the feature is absent, and preprocessing choices can affect what features are shown. However, this does become a practical problem if the PCA is used as part of an unsupervised workflow, such as segmentation or k -means, or if trying to filter out the positional modes based on variance or energy. See Fig. S12 for feature PCAs with scaling.

4.3 Feature properties: robustness, similarity, decomposition

The features of DINOv2 have many desirable properties: wide applicability, robustness across ‘changes of pose, style or even objects’ and meaningful unsupervised decompositions (via PCA or k -means) [7]. We explore some of these properties in Fig. 6 and Fig. S13.

Fig. 6 (a) shows the cosine similarity for a given query point (red patch) for DINOv2 and our ALiBi-Dv2. For heterogeneous natural images the results are similar, but for out-of-distribution homogeneous images like an

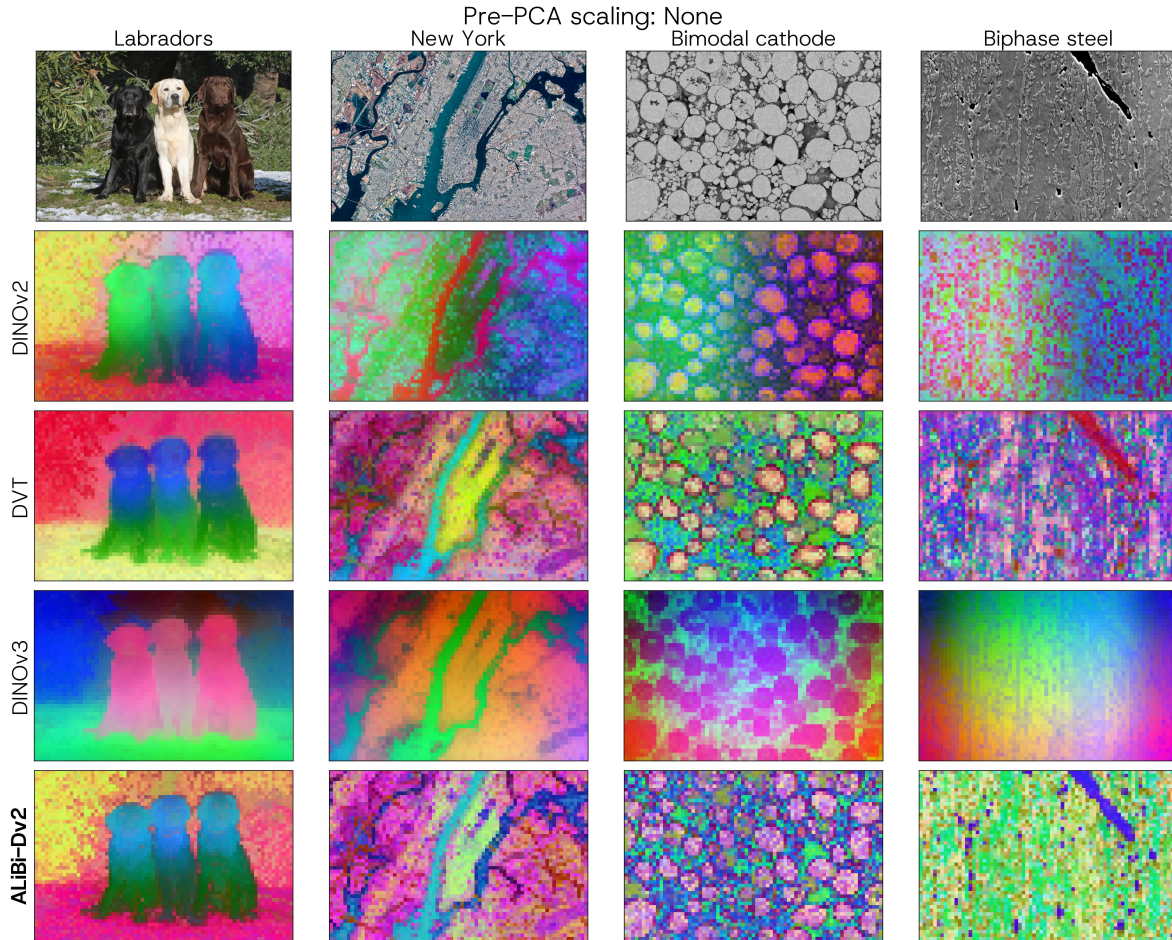


Figure 5: Feature PCA visualisations for DINOv2, DINOv3 and our ALiBi-Dv2. We retain desirable object decompositions (e.g. head vs body of the dogs), whilst having less positional features for the satellite image and the SEM images of a battery cathode [51] & biphase steel [54].

SEM image of a battery cathode ALiBi-Dv2 has a far more homogenous response.

We show the k -means [56] based decompositions for the DINOv2, DVT and ALiBi-Dv2 features of a set of natural images in Fig. 6 (b). Features were scaled (zero-mean, unit standard deviation) channel-wise prior to clustering with 15 initializations, and all 384 output features were used. For natural images the results are similar, but for some images (bubbles, eutectic steel alloy [55]), DINOv2 and DVT can decompose on positional information, either vertically or radially; as mentioned previously, DVT tends to split vertically. In contrast, our ALiBi-Dv2 decomposes homogeneously.

Note these examples were selected to demonstrate positional decomposition; for in-distribution heterogeneous images, the features and subsequent decompositions for DINOv2 and especially DVT are generally of high-quality.

Model	VOC07	VOC12	ADE20k
DINOv2	0.680	0.762	0.240
NoPE	0.689	0.757	0.235
ALiBi-Dv2	0.692	0.769	0.239

Table 3: Validation mIoU (mean Intersection over Union) for frozen-feature linear probe semantic segmentation of benchmark datasets. We see our ALiBi-Dv2 performs similarly to, and in some cases outperforms, DINOv2.

4.4 Benchmarking semantic segmentation

To further assess whether our ALiBi-Dv2 retains useful DINOv2 semantics, we train linear probes atop frozen ViT features across a series of benchmark segmentation datasets. Linear probe training was similar to previous works [7, 15]: bilinear upsampling of output features followed by a linear layer and batch norm. Note the probes were trained for a relatively short period compared to other works, hence lower mIoUs. The full training setup is described in Sec. S7.1.

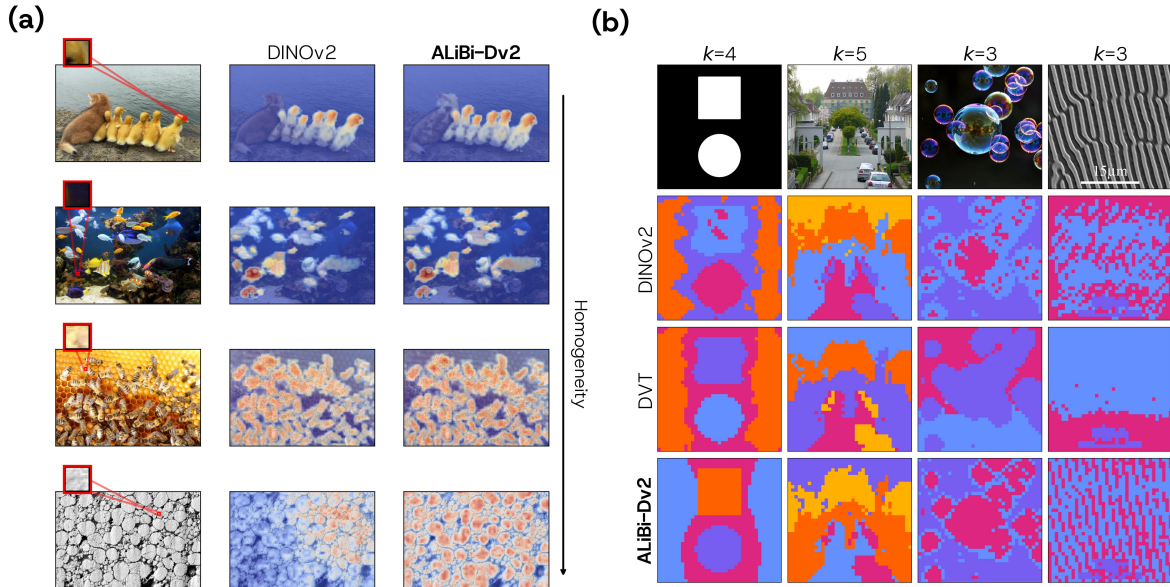


Figure 6: (a) Cosine similarity scores for DINOv2 and our ALiBi-Dv2 for a given query patch (red inset square). ALiBi-Dv2 has more uniform similarities for increasingly homogenous (and out-of-distribution) images, such as the SEM image of a Li-ion battery cathode [51]. (b) k -means clustering of features of DINOv2-S, DVT and our ALiBi-Dv2. For some images, like the SEM micrograph of a eutectic alloy [55], both DINOv2 and DVT decompose using positional information (radial or vertical), whereas ALiBi-Dv2 produces a clean, homogeneous result.

Tab. 3 contains the validation mIoU for linear probes trained on the VOC07 [57], VOC12 [58] and ADE20K [59] datasets for DINOv2, NoPE and ALiBi-Dv2. We see that ALiBi-Dv2 either performs similarly to or better than DINOv2 and NoPE, indicating that the model retains both general semantics and the ability to model long-range interactions. Some example predictions are shown in Fig. S14.

The improved performance of ALiBi-Dv2 could be attributed to either improved homogeneity (probes may previously have fit to positional information) or mild artefact removal. NoPE performs remarkably well; it seems generally able to construct objects from patch-patch similarity and continuity. Sec. S3 however contains some examples where this is not the case. We also measure the performance of probes under input image transformations such as translations with wrapped boundaries, flips and rotations, this can be found in Tab. S3.

4.5 Applied to trainable segmentation

One area where more homogeneous ViT features are important is trainable segmentation of materials science micrographs. The trainable segmentation paradigm is useful for researchers because it allows flexible class definitions, works with very sparse label data and trains quickly [41, 42]. These segmentations are necessary to perform quantitative analysis of materials, from ba-

sic properties like particle size and distribution [60], to correlating with device performance (yield strength, battery charging speed, degradation) and finally to end-to-end optimisation of the manufacturing workflow [61].

Following Refs. [26] and [27], we perform trainable segmentation for a set of images using DINOv2, DVT and ALiBi-Dv2 features. The corresponding ViT features are scaled, reduced to 9 dimensions via PCA and then are bilinearly upsampled to match image dimensions. Next we concatenate these with the classical features for that image (*i.e.* a collection of multiscale blurs, edge detectors - see Sec. S8.1). Finally we train an XGBoost classifier [62] to map from the features of labelled pixels to their class, followed by conditional random field (CRF) post-processing [63]. The labels, classical features and classifier parameters were the same for each image - the only difference was the choice of ViT features. The predictions are shown in Fig. 7.

There is little difference for the natural image, however the differences for the microstructural images (SEM images of a Li-ion battery cathode [64] and silicon-graphite anode [51]) are stark. Segmentations using DINOv2 and DVT features are clearly positionally biased, failing to predict classes either in the centre or bottom of the images. DINOv2's left-to-right bias and DVT's up-to-down bias (quantified in Sec. 4.1) are apparent. The ALiBi-Dv2 predictions are far more homogeneous.

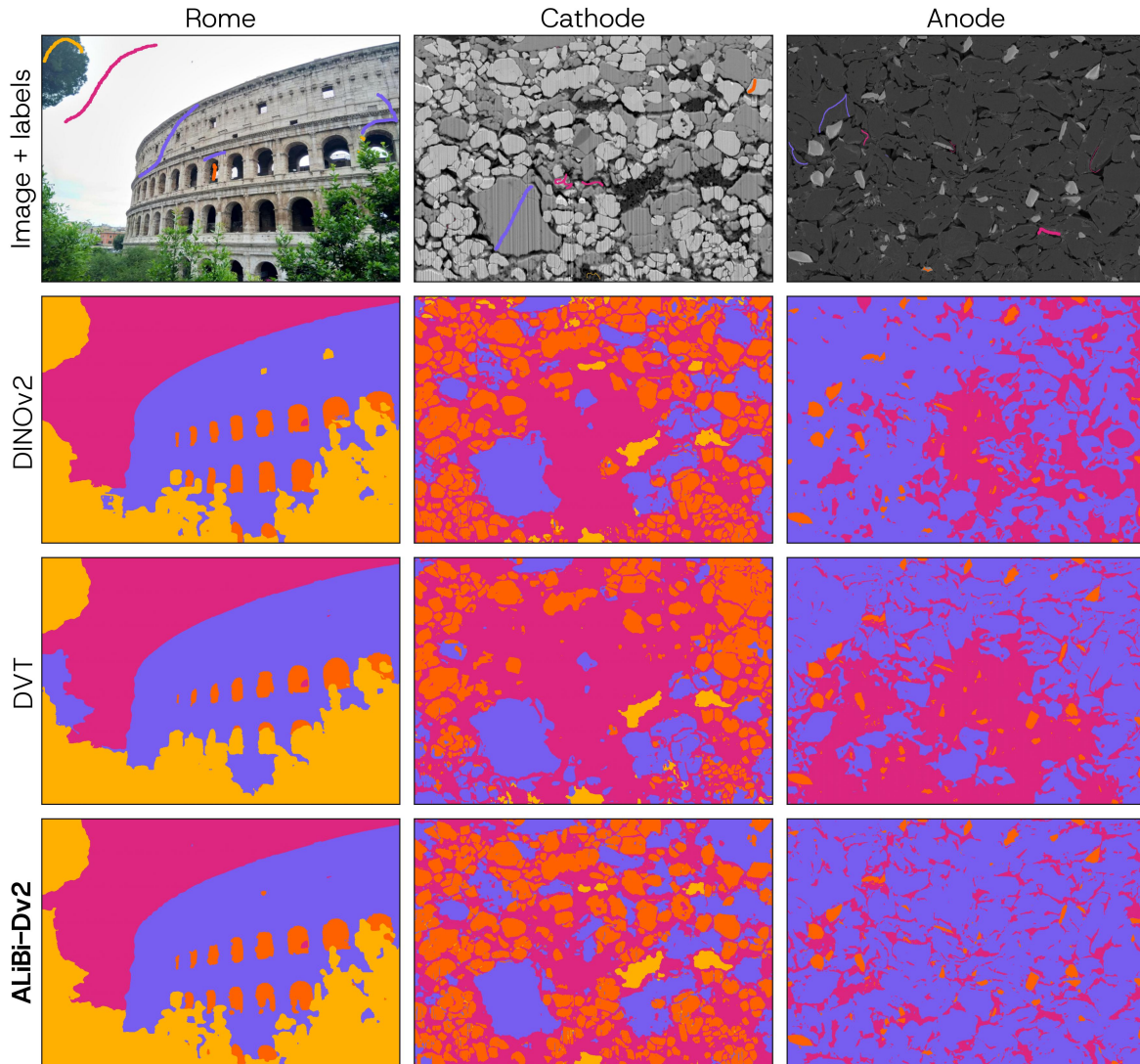


Figure 7: Trainable segmentation of images: a set of features that describe each pixel (classical + bilinearly upsampled ViT features) are extracted, and a lightweight classifier (XGBoost) is trained to map from feature vectors to user labels. Our ALiBi-Dv2 has more homogenous features and so produces less positionally biased (and therefore higher quality) segmentations of complex microstructures. Segmentations using DINOv2 and DVT’s features are biased either radially, horizontally or vertically.

The key difficulty in segmenting these battery materials is capturing the ‘pore-back’ effect [47]. Researchers typically create flat cross-sections by ablating or milling an area with an ion beam or laser before imaging with their electron microscope. However, batteries are porous materials (*i.e.* have gaps in their structure - important for transport) and when researchers image cross-sections, closely-located material from further ‘down’ the sample can appear in the same level cross-section image.

The goal is to correctly segment this out-of-plane or ‘pore-back’ material as pore - otherwise statistics become skewed and later simulations non-physical. ViT features have previously proved useful at capturing the

in-plane vs out-of-plane distinction where classical features previously struggled. However, if positional information is fit to instead, or is intermixed in the ViT’s representation of in- and out- of plane material, then poor segmentation results are obtained.

We note these labels are, in a sense, adversarial in that they are very sparse and spread across the image. More labels, placed closer together can improve performance for the other ViT features. The ‘pore-back’ effect is just one example of where ViTs can improve materials image analysis - we include further examples in Fig. S15, as well as a quantitative benchmark in Fig. S16. All benefit from the improved homogeneity of ALiBi-Dv2.

5 Conclusion

In summary, we have examined positional biases in feature foundation models, finding them present across a range of training objectives and positional encodings. These biases tend to be linearly decodable, often manifesting as simple ramps in the output features whose channel-order is consistent across different images.

The difficulty in removing these biases motivated us to train a DINOv2 checkpoint with ALiBi positional encodings. We found that biased DINOv2 embeddings could be used as a training target to produce a homogeneous ALiBi-Dv2 model. Once trained, we showed this model produced rich features that retained the semantics and useful properties of DINOv2 without the problematic positional biases. This meant it could be applied successfully to trainable segmentation of complex microscopy images that previous models struggled with.

Whilst we found it possible to finetune an existing DINOv2 checkpoint with ALiBi encodings, we did not explore whether it is possible to train a model like DINOv2 from scratch with ALiBi positional encoding. We also found evidence that this positional bias was a more general property of self-supervision (rather than being isolated to the DINO objective or learned positional encodings), but we have yet to explain why. Both questions represent interesting future work.

Code Availability

The code needed to reproduce the results of the paper is available at <https://github.com/tldr-group/dino-saw> with an MIT license agreement.

Acknowledgements

This work was supported by funding from the the EPSRC and SFI Centre for Doctoral Training in Advanced Characterisation of Materials (EP/S023259/1 received by RD), the Royal Society (IF\R2\222059 received by AV as a Royal Society Industry Fellow) and the EPSRC Open Plus Fellowship "AIMS-DEEP" (Award UKRI4070 received by SJC).

AB, AW and MP thank the German Ministry for Research, Technology and Space (BMFTR) for funding the SiMba project (03XP0584).

The authors would like to thank other members of the TLDR group for their testing and feedback.

Authorship

MP, SJC, AV and RD conceptualised the project. MP and RD wrote the code and performed the experiments. AV, AW, AB and SJC contributed to the development of the concepts presented in the work, and provided funding & equipment access. AV, AW, AB, SJC and RD provided supervision during the project. All authors contributed to revisions and edits of the manuscript.

Competing interests

The authors declare no competing interests.

References

- [1] X. Wang, L. Miao, and Z. Zhou, "CoCAViT: Compact Vision Transformer with Robust Global Coordination," *arXiv preprint, arXiv:2508.05307*, 2025.
- [2] A. Radford, J. W. Kim, C. Hallacy, A. Ramesh, G. Goh, S. Agarwal, G. Sastry, A. Askell, P. Mishkin, and J. Clark, "Learning transferable visual models from natural language supervision," in *International conference on machine learning*, pp. 8748–8763, PMLR, 2021. Type: Conference Proceedings.
- [3] X. Zhai, A. Kolesnikov, N. Houlsby, and L. Beyer, "Scaling Vision Transformers," *arXiv preprint, arXiv:2106.04560*, 2022.
- [4] K. He, X. Chen, S. Xie, Y. Li, P. Dollár, and R. Girshick, "Masked Autoencoders Are Scalable Vision Learners," *arXiv preprint, arXiv:2111.06377*, 2021.
- [5] J. Zhou, C. Wei, H. Wang, W. Shen, C. Xie, A. Yuille, and T. Kong, "iBOT: Image BERT Pre-Training with Online Tokenizer," *arXiv preprint, arXiv:2111.07832*, 2022.
- [6] M. Caron, H. Touvron, I. Misra, H. Jégou, J. Mairal, P. Bojanowski, and A. Joulin, "Emerging Properties in Self-Supervised Vision Transformers," *arXiv preprint, arXiv:2104.14294*, 2021.
- [7] M. Oquab, T. Darcet, T. Moutakanni, H. Vo, M. Szafraniec, V. Khalidov, P. Fernandez, D. Haziza, F. Massa, A. El-Nouby, M. Assran, N. Ballas, W. Galuba, R. Howes, P.-Y. Huang, S.-W. Li, I. Misra, M. Rabbat, V. Sharma, G. Synnaeve, H. Xu, H. Jegou, J. Mairal, P. Labatut, A. Joulin, and P. Bojanowski, "DINOv2: Learning Robust Visual Features without Supervision," *arXiv preprint, arXiv:2304.07193*, 2023.

- [8] O. Siméoni, H. V. Vo, M. Seitzer, F. Baldassarre, M. Oquab, C. Jose, V. Khalidov, M. Szafraniec, S. Yi, M. Ramamonjisoa, F. Massa, D. Haziza, L. Wehrstedt, J. Wang, T. Darcet, T. Moutakanni, L. Sentana, C. Roberts, A. Vedaldi, J. Tolan, J. Brandt, C. Couprie, J. Mairal, H. Jégou, P. Labatut, and P. Bojanowski, “DINOv3,” *arXiv preprint, arXiv:2508.10104*, 2025.
- [9] M. Assran, Q. Duval, I. Misra, P. Bojanowski, P. Vincent, M. Rabbat, Y. LeCun, and N. Ballas, “Self-Supervised Learning from Images with a Joint-Embedding Predictive Architecture,” *arXiv preprint, arXiv:2301.08243*, 2023.
- [10] P. Engstler, L. Melas-Kyriazi, C. Rupprecht, and I. Laina, “Understanding Self-Supervised Features for Learning Unsupervised Instance Segmentation,” *arXiv preprint, arXiv:2311.14665*, 2023.
- [11] S. Amir, Y. Gandelsman, S. Bagon, and T. Dekel, “Deep ViT Features as Dense Visual Descriptors,” *arXiv preprint, arXiv:2112.05814*, 2022.
- [12] A. Kirillov, E. Mintun, N. Ravi, H. Mao, C. Rolland, L. Gustafson, T. Xiao, S. Whitehead, A. C. Berg, W.-Y. Lo, P. Dollár, and R. Girshick, “Segment Anything,” *arXiv preprint, arXiv:2304.02643*, 2023.
- [13] Q. Sun, Y. Fang, L. Wu, X. Wang, and Y. Cao, “EVA-CLIP: Improved Training Techniques for CLIP at Scale,” *arXiv preprint, arXiv:2303.15389*, 2023.
- [14] T. Darcet, M. Oquab, J. Mairal, and P. Bojanowski, “Vision Transformers Need Registers,” *arXiv preprint, arXiv:2309.16588*, 2023.
- [15] J. Yang, K. Z. Luo, J. Li, C. Deng, L. Guibas, D. Krishnan, K. Q. Weinberger, Y. Tian, and Y. Wang, “Denoising Vision Transformers,” *arXiv preprint, arXiv:2401.02957*, 2024.
- [16] T. Fel, B. Wang, M. A. Lepori, M. Kowal, A. Lee, R. Balestrierio, S. Joseph, E. S. Lubana, T. Konkle, D. Ba, and M. Wattenberg, “Into the Rabbit Hull: From Task-Relevant Concepts in DINO to Minkowski Geometry,” *arXiv preprint, arXiv:2510.08638*, 2025.
- [17] F. R. Doshi, T. Fel, T. Konkle, and G. Alvarez, “Bi-Orthogonal Factor Decomposition for Vision Transformers,” *arXiv preprint, arXiv:2601.05328*, 2026.
- [18] O. Siméoni, G. Puy, H. V. Vo, S. Roburin, S. Gidaris, A. Bursuc, P. Pérez, R. Marlet, and J. Ponce, “Localizing Objects with Self-Supervised Transformers and no Labels,” *arXiv preprint, arXiv:2109.14279*, 2021.
- [19] S. S. Rambhatla, I. Misra, R. Chellappa, and A. Shrivastava, “MOST: Multiple Object localization with Self-supervised Transformers for object discovery,” *arXiv preprint, arXiv:2304.05387*, 2023.
- [20] O. Siméoni, E. Zablocki, S. Gidaris, G. Puy, and P. Pérez, “Unsupervised Object Localization in the Era of Self-Supervised ViTs: A Survey,” *arXiv preprint, arXiv:2310.12904*, 2023.
- [21] L. Melas-Kyriazi, C. Rupprecht, I. Laina, and A. Vedaldi, “Deep Spectral Methods: A Surprisingly Strong Baseline for Unsupervised Semantic Segmentation and Localization,” *arXiv preprint, arXiv:2205.07839*, 2022.
- [22] Y. Wang, X. Shen, Y. Yuan, Y. Du, M. Li, S. X. Hu, J. L. Crowley, and D. Vaufreydaz, “TokenCut: Segmenting Objects in Images and Videos with Self-supervised Transformer and Normalized Cut,” *arXiv preprint, arXiv:2209.00383*, 2023.
- [23] Y. Wang, X. Shen, S. Hu, Y. Yuan, J. Crowley, and D. Vaufreydaz, “Self-Supervised Transformers for Unsupervised Object Discovery using Normalized Cut,” *arXiv preprint, arXiv:2202.11539*, 2022.
- [24] M. Seifi, D. Dalle Nogare, J. M. Battagliotti, V. Galinova, A. K. Rao, P.-H. Jouneau, A. Archit, F. Beuttenmueller, D. Dörr, M. G. Ferreira, C. Fuster-Barceló, V. Galinova, C. García-López-de Haro, E. Gómez-de Mariscal, M. Hartley, R. Henriques, I. Hidalgo-Cenalmor, F. Jug, A. Kreshuk, E. Lundberg, N. Mechtel, A. Muñoz-Barrutia, W. Ouyang, C. Pape, C. T. Russell, M. Seifi, B. Serrano-Solano, T. Vieira, T. Zulueta-Coarasa, C. Pape, J. Decelle, F. Jug, J. Deschamps, and AI4Life Horizon Europe Programme Consortium, “FeatureForest: the power of foundation models, the usability of random forests,” *npj Imaging*, vol. 3, p. 32, July 2025.
- [25] L. Hinderling, G. Witz, R. Schwob, A. Stojilković, M. Dobrzyński, M. Vladymyrov, J. Frei, B. Grädel, A. Frismantiene, and O. Pertz, “Convpaint - Interactive pixel classification using pre-trained neural networks,” *bioRxiv*, 2024.
- [26] R. Docherty, A. Vamvakeros, and S. J. Cooper, “Upsampling DINOv2 Features for Unsupervised Vision Tasks and Weakly Supervised Materials Segmentation,” *Advanced Intelligent Systems*, p. e202501094, 2026.
- [27] R. Docherty, A. Vamvakeros, and S. J. Cooper, “Maybe you don’t need a U-Net: convolutional feature upsampling for materials micrograph segmentation,” *arXiv preprint, arXiv:2508.21529*, 2025.

- [28] L. Himanen, A. Geurts, A. S. Foster, and P. Rinke, “Data-Driven Materials Science: Status, Challenges, and Perspectives,” *Advanced science (Weinheim, Baden-Wurtemberg, Germany)*, vol. 6, p. 1900808, Nov. 2019.
- [29] S. E. Whitman and M. I. Latypov, “Machine learning of microstructure–property relationships in materials with robust features from foundational vision transformers,” *arXiv preprint, arXiv:2501.18637*, 2025.
- [30] O. Press, N. A. Smith, and M. Lewis, “Train Short, Test Long: Attention with Linear Biases Enables Input Length Extrapolation,” *arXiv preprint, arXiv:2108.12409*, 2022.
- [31] F. Al-Khateeb, N. Dey, D. Soboleva, and J. Hestness, “Position Interpolation Improves ALiBi Extrapolation,” *arXiv preprint, arXiv:2310.13017*, 2023.
- [32] A. Vaswani, N. Shazeer, N. Parmar, J. Uszkoreit, L. Jones, A. N. Gomez, L. Kaiser, and I. Polosukhin, “Attention is all you need,” *Advances in neural information processing systems*, vol. 30, 2017. Type: Journal Article.
- [33] M. Phuong and M. Hutter, “Formal Algorithms for Transformers,” *arXiv preprint, arXiv:2207.09238*, 2022.
- [34] A. Dosovitskiy, L. Beyer, A. Kolesnikov, D. Weissenborn, X. Zhai, T. Unterthiner, M. Dehghani, M. Minderer, G. Heigold, S. Gelly, J. Uszkoreit, and N. Houlsby, “An Image is Worth 16x16 Words: Transformers for Image Recognition at Scale,” *arXiv preprint, arXiv:2010.11929*, 2021.
- [35] M. Tancik, P. P. Srinivasan, B. Mildenhall, S. Fridovich-Keil, N. Raghavan, U. Singhal, R. Ramamoorthi, J. T. Barron, and R. Ng, “Fourier Features Let Networks Learn High Frequency Functions in Low Dimensional Domains,” *arXiv preprint, arXiv:2006.10739*, 2020.
- [36] J. Su, Y. Lu, S. Pan, A. Murtadha, B. Wen, and Y. Liu, “RoFormer: Enhanced Transformer with Rotary Position Embedding,” *arXiv preprint, arXiv:2104.09864*, 2023.
- [37] Y. Li, C.-Y. Wu, H. Fan, K. Mangalam, B. Xiong, J. Malik, and C. Feichtenhofer, “MViTv2: Improved Multiscale Vision Transformers for Classification and Detection,” *arXiv preprint, arXiv:2112.01526*, 2022.
- [38] A. Fuller, K. Millard, and J. R. Green, “CROMA: Remote Sensing Representations with Contrastive Radar-Optical Masked Autoencoders,” *arXiv preprint, arXiv:2311.00566*, 2023.
- [39] H. Li, Y. Zhang, C. Zhu, J. Cai, S. Zheng, and L. Yang, “Long-MIL: Scaling Long Contextual Multiple Instance Learning for Histopathology Whole Slide Image Analysis,” *arXiv preprint, arXiv:2311.12885*, 2023.
- [40] F. Baldassarre, “Ablation on positional embeddings,” <https://github.com/facebookresearch/dinov3/issues/17>.
- [41] I. Arganda-Carreras, V. Kaynig, C. Rueden, K. W. Eliceiri, J. Schindelin, A. Cardona, and H. Sebastian Seung, “Trainable Weka Segmentation: a machine learning tool for microscopy pixel classification,” *Bioinformatics*, vol. 33, pp. 2424–2426, Aug. 2017.
- [42] S. Berg, D. Kutra, T. Kroeger, C. N. Straehle, B. X. Kausler, C. Haubold, M. Schiegg, J. Ales, T. Beier, M. Rudy, K. Eren, J. I. Cervantes, B. Xu, F. Beuttenmueller, A. Wolny, C. Zhang, U. Koethe, F. A. Hamprecht, and A. Kreshuk, “ilastik: interactive machine learning for (bio)image analysis,” *Nature Methods*, Sept. 2019.
- [43] C. Li, X. Ma, J. Deng, J. Li, Y. Liu, X. Zhu, J. Liu, and P. Zhang, “Machine learning-based automated fungal cell counting under a complicated background with ilastik and ImageJ,” *Engineering in Life Sciences*, vol. 21, no. 11, pp. 769–777, 2021.
- [44] E. Owembabazi, I. M. Usman, and W. Makena, “Segmentation and quantification of testicular histology images using machine learning bioimage analysis tools; Ilastik and Fiji software,” *MethodsX*, vol. 15, p. 103503, 2025.
- [45] D. S. Bulgarevich, S. Tsukamoto, T. Kasuya, M. Demura, and M. Watanabe, “Automatic steel labeling on certain microstructural constituents with image processing and machine learning tools,” *Science and Technology of Advanced Materials*, vol. 20, no. 1, pp. 532–542, 2019.
- [46] R. Lasnel, L. Frouté, A. R. Kovscek, I. C. Jolivet, and P. Creux, “Image processing and segmentation open source codes applied to FIB-SEM images of ultra-tight gas shales samples: Enhanced pore space representativeness and mineral identification,” *Gas Science and Engineering*, vol. 138, p. 205610, 2025.
- [47] S. J. Cooper, S. A. Roberts, Z. Liu, and B. Winiarski, “Methods—Kintsugi Imaging of Battery Electrodes: Distinguishing Pores from the Carbon Binder Domain using Pt Deposition,” *Journal of The Electrochemical Society*, vol. 169, p. 070512, July 2022.
- [48] J. Stuckner, B. Harder, and T. M. Smith, “Microstructure segmentation with deep learning encoders pre-trained on a large microscopy dataset,”

- npj Computational Materials*, vol. 8, p. 200, Sept. 2022.
- [49] M. Cimpoi, S. Maji, I. Kokkinos, S. Mohamed, , and A. Vedaldi, “Describing textures in the wild,” in *Proceedings of the IEEE Conf. on Computer Vision and Pattern Recognition (CVPR)*, 2014.
- [50] H. Caesar, J. Uijlings, and V. Ferrari, “COCO-Stuff: Thing and Stuff Classes in Context,” *arXiv preprint, arXiv:1612.03716*, 2018.
- [51] R. Docherty, S. Riley, J. D. Morley, E. Papoutsellis, A. D. Bobitan, J. Donoghue, K. Rankin, F. A. Borges, L. Salinas-Farran, S. Michalik, A. Liptak, G. Burca, P.-O. Autran, J. Wright, W. Kockelmann, O. Gutowski, A.-C. Dippel, M. v. Zimmermann, D. Matras, B. Winiarski, J. Mangum, M. Popeil, D. P. Finegan, J. A. Gott, D. Propprentner, G. West, L. F. J. Piper, H. Dong, M. P. Jones, F. Iacoviello, A. V. Llewellyn, R. Jervis, Y. Kimura, K. Amezawa, O. Sekizawa, M. G. Ardakani, A. Omirkhan, M. P. Ryan, J. O. Douglas, S. Wang, F. Giuliani, N. Mulcahy, S. Conroy, C. George, A. M. Beale, S. D. M. Jacques, S. J. Cooper, and A. Vamvakeros, “Battery Imaging Library: Multi-length scale and multi-modal synchrotron and laboratory battery imaging data for all,” *ChemRxiv*, vol. 2026, no. 0223, 2026.
- [52] H. Touvron, M. Cord, M. Douze, F. Massa, A. Sablayrolles, and H. Jégou, “Training data-efficient image transformers & distillation through attention,” *arXiv preprint, arXiv:2012.12877*, 2021.
- [53] Y. Fang, Q. Sun, X. Wang, T. Huang, X. Wang, and Y. Cao, “EVA-02: A visual representation for neon genesis,” *Image and Vision Computing*, vol. 149, p. 105171, Sept. 2024.
- [54] S. Medghalchi, J. Kortmann, S.-H. Lee, E. Karimi, U. Kerzel, and S. Korte-Kerzel, “Automated segmentation of large image datasets using artificial intelligence for microstructure characterisation and damage analysis,” *Materials & Design*, vol. 243, p. 113031, 2024.
- [55] “DoITPoMS micrograph library.” <https://www.doitpoms.ac.uk/index.php>.
- [56] F. Pedregosa, G. Varoquaux, A. Gramfort, V. Michel, B. Thirion, O. Grisel, M. Blondel, P. Prettenhofer, R. Weiss, V. Dubourg, J. Vanderplas, A. Passos, D. Cournapeau, M. Brucher, M. Perrot, and E. Duchesnay, “Scikit-learn: Machine Learning in Python,” *Journal of Machine Learning Research*, vol. 12, pp. 2825–2830, 2011.
- [57] M. Everingham, L. Van Gool, C. K. I. Williams, J. Winn, and A. Zisserman, “The PASCAL Visual Object Classes Challenge 2007 (VOC2007) Results.”
- [58] M. Everingham, L. Van Gool, C. K. I. Williams, J. Winn, and A. Zisserman, “The PASCAL Visual Object Classes Challenge 2012 (VOC2012) Results.”
- [59] B. Zhou, H. Zhao, X. Puig, T. Xiao, S. Fidler, A. Barriuso, and A. Torralba, “Semantic Understanding of Scenes through the ADE20K Dataset,” *arXiv preprint, arXiv:1608.05442*, 2018.
- [60] F. L. E. Usseglio-Viretta and K. Smith, “Quantitative Microstructure Characterization of a NMC Electrode,” *ECS Transactions*, vol. 77, p. 1095, July 2017.
- [61] S. Kench, I. Squires, A. Dahari, F. Brosa Planella, S. A. Roberts, and S. J. Cooper, “Li-ion battery design through microstructural optimization using generative AI,” *Matter*, vol. 7, pp. 4260–4269, Dec. 2024.
- [62] T. Chen and C. Guestrin, “XGBoost: A Scalable Tree Boosting System,” in *Proceedings of the 22nd ACM SIGKDD International Conference on Knowledge Discovery and Data Mining, KDD ’16*, pp. 785–794, ACM, Aug. 2016.
- [63] P. Krähenbühl and V. Koltun, “Efficient Inference in Fully Connected CRFs with Gaussian Edge Potentials,” *arXiv preprint, arXiv:1210.5644*, 2012.
- [64] “Biphase cathode sem.” <https://forum.image.sc/t/three-phase-segmentation-of-sem-image/92812>.
- [65] N. Prakash, P. Gasper, and F. Usseglio-Viretta, “ExpertSegmentation: Segmentation for microscopy with domain-informed targets via custom loss,” *Acta Materialia*, vol. 291, p. 120993, 2025.

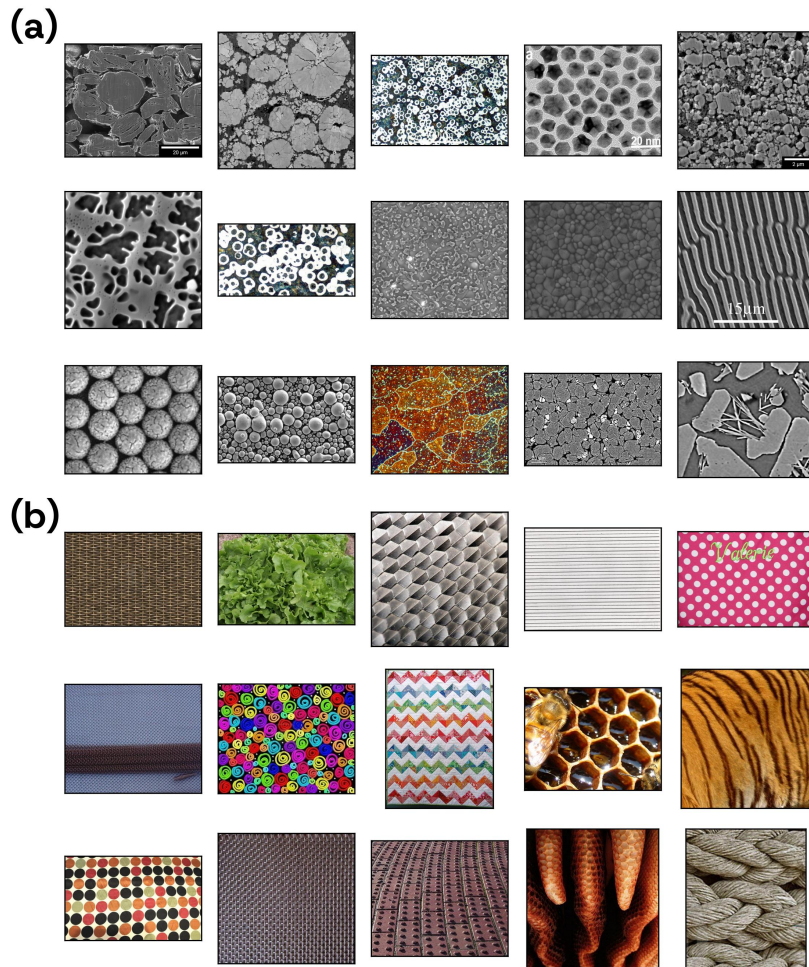


Figure S1: (a) Micrographs used for the linear probe. (b) Random samples from the DTD used for the linear probe [49].

Supplementary

S1 Linear probe details

S1.1 Dataset examples

We show examples for the linear probe datasets in Fig. S1. Note that some images from the texture dataset [49] are not perfectly homogenous, having either spatially biased content, or colour / contrast / depth gradients. These could be fit to in principle, and may be why our ALiBi-Dv2 has a higher R^2 score on DTD compared to random noise or micrographs.

S1.2 Sampling strategies

To check the influence of different sampling methods, we compare different strategies: grid-based interpolation, grid-based interpolation with holdout regions for extrapolation, and random sampling.

No significant differences between the different sampling strategies are observed. Only minor deviations appear for the grid_holdout setting compared to the others. This may be explained by the presence of the holdout region, which provides less information about the ramp compared to the other approaches.

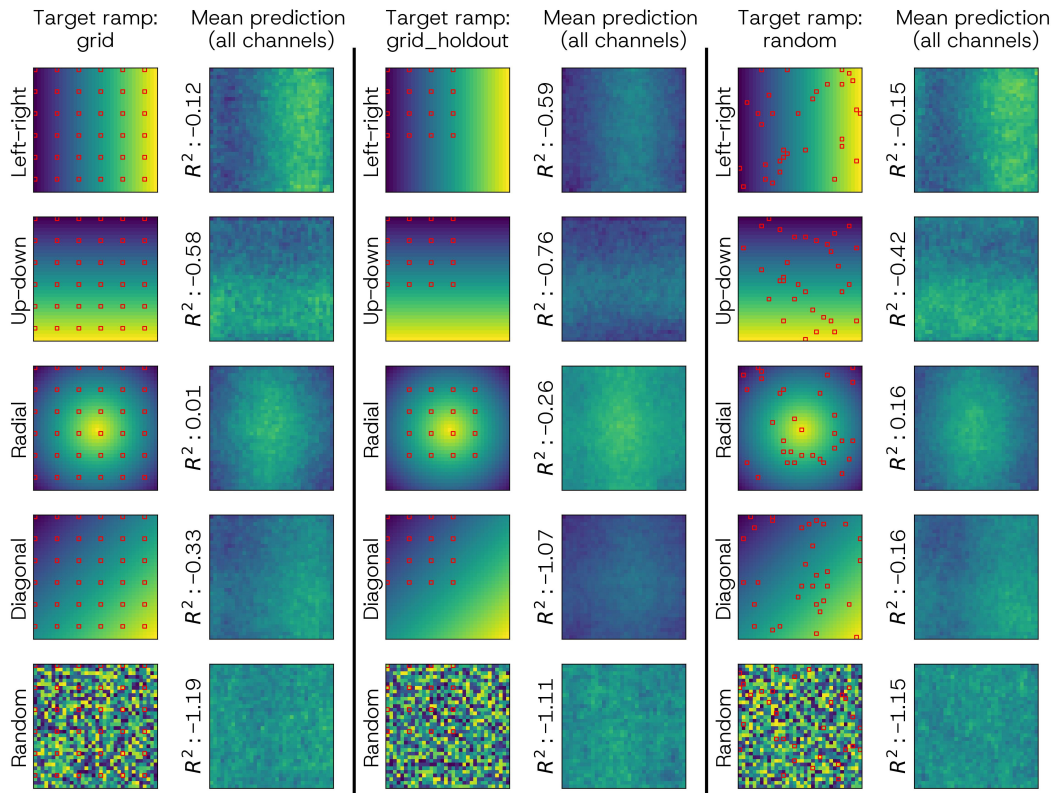


Figure S2: Comparison of sampling strategies. For each method (grid, grid_holdout, random), the target ramps (left) and the mean model predictions across all channels (right) are shown. Red markers denote sampled training locations.

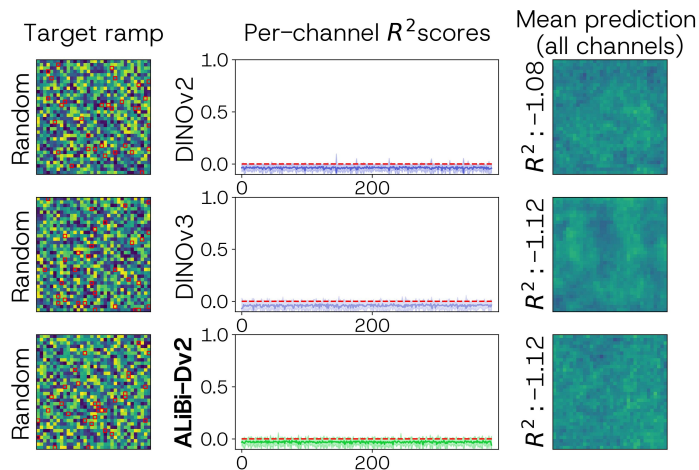


Figure S3: Linear probe analysis of DINOv2, DINOv3 and ALiBi-Dv2 with a target ramp of random noise, using the micrograph dataset.

S1.3 Random ramp results

To confirm our linear probing is not fitting to spurious correlations in the features, we attempt to fit to a random noise ramp, plotting the results in Fig. S3. We see low R^2 scores for all models.

S1.4 Results on additional models

We present linear probe analysis of ViT features for additional models in Fig. S4 and Fig. S5 (ViT-B MAE & our ALiBi-Dv2 respectively). Again we note highly-positional (ramp-like) outlier channels, indicating this

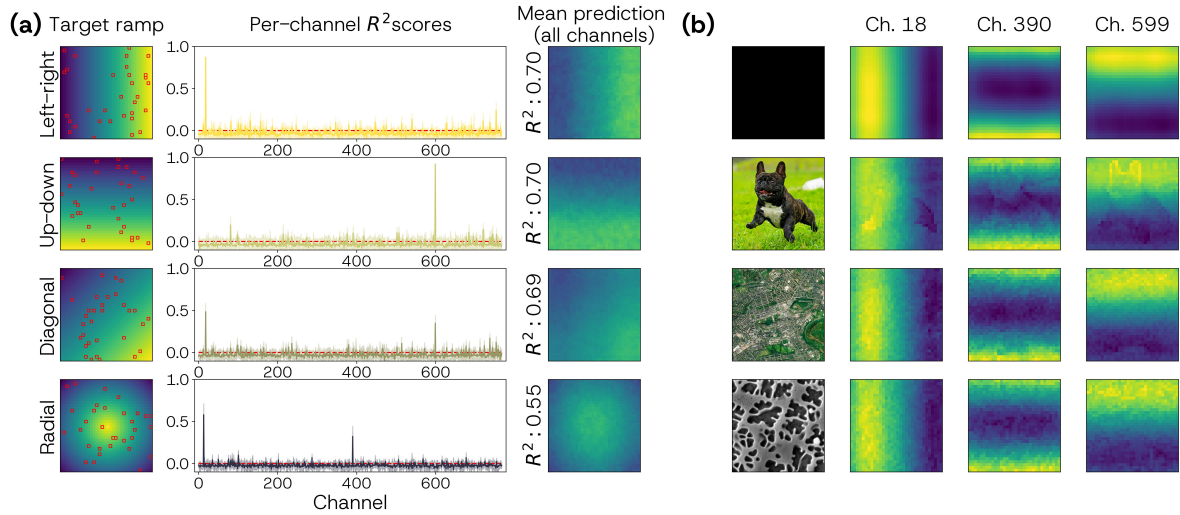


Figure S4: Linear probe analysis of ViT-B (MAE) features over the micrograph dataset. Again we see clear ramp channels in the output features.

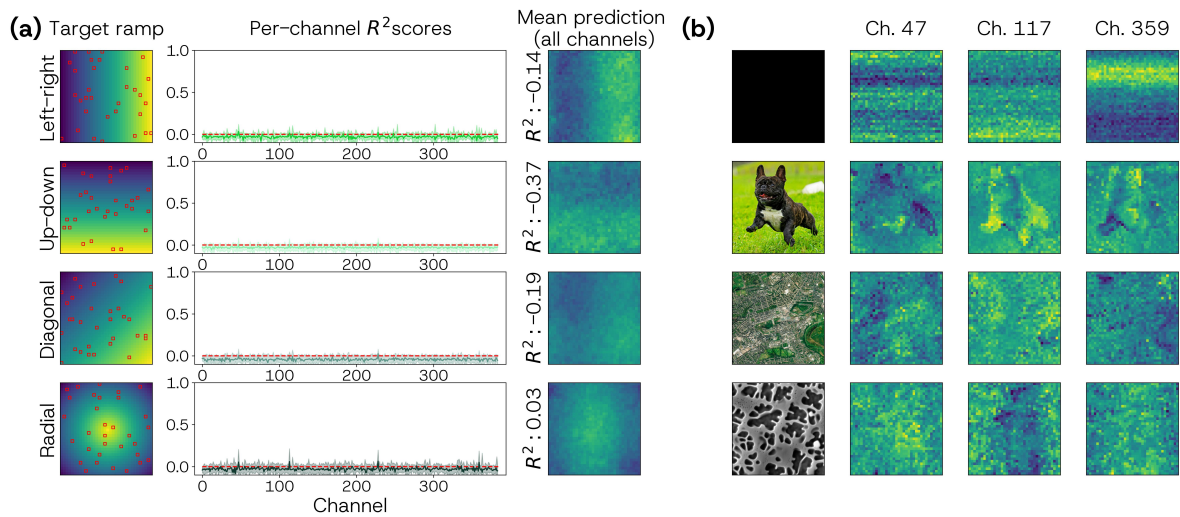


Figure S5: Linear probe analysis of our ALiBi-Dv2 features over the micrograph dataset.

phenomenon is not limited to the DINO training objective. Our ALiBi-Dv2 model does not show these outlier channels, and its mean prediction scores (when training on all channels) are consistently low.

S1.5 Layer channel-behaviour of models

We performed channel-wise linear probing (targeting an (x, y) ramp) as a function of layer for a series of literature ViT backbones, presenting the result in Fig. S6.

We note two things: first, SSL backbones have stronger and more widespread positional information compared to supervised models (ViT-B-INet, CLIP-B) and second that DINOv3 becomes more positional as layers increase, whereas DINO and DINOv2 become less positional. DINO and DINOv2 use learned positional encodings, added at the start of the model, whereas DINOv3 uses RoPE, which is applied at each attention layer.

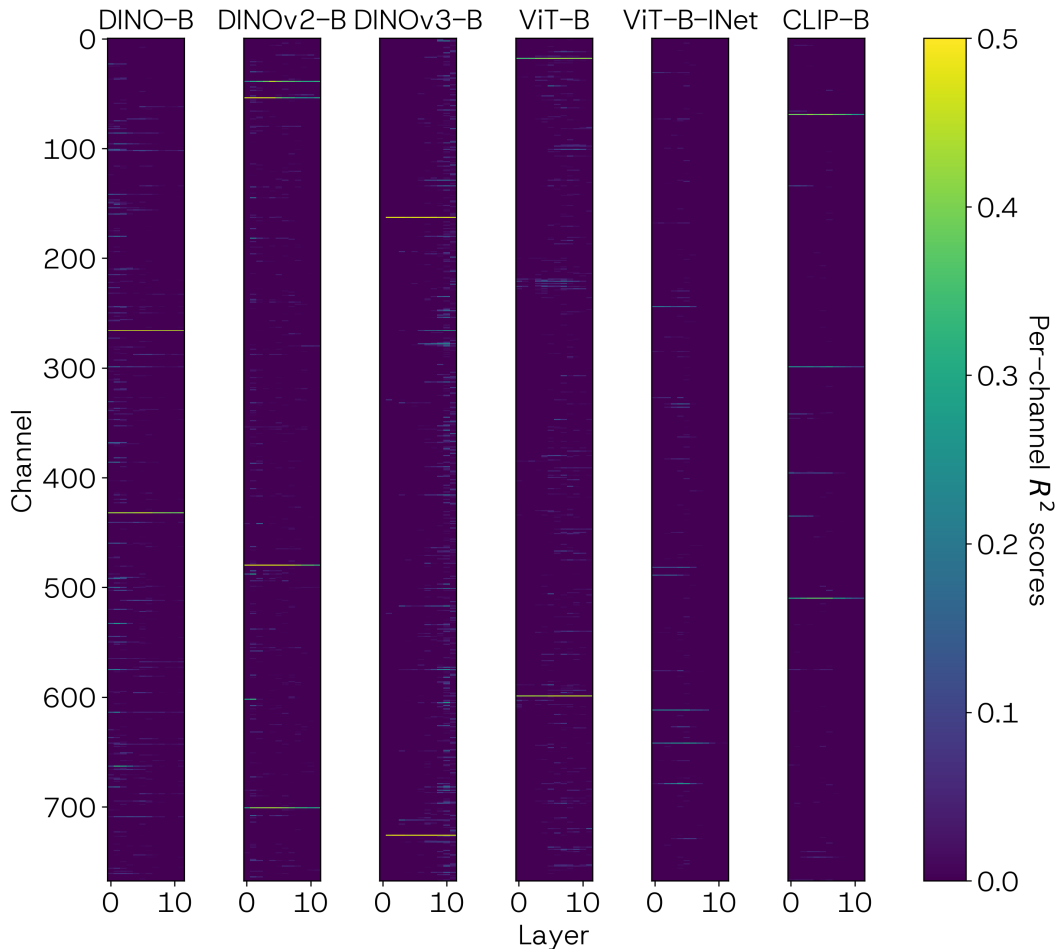


Figure S6: Per-channel per-layer R^2 scores for an (x, y) ramp for a series of models. We see self-supervised models (DINO-B, DINOv2-B, DINOv3-B, ViT-B) have stronger and more widespread positional channels.

ALiBi-Dv2	low resolution	high resolution
image size	(224, 224)	(518, 518)
learning rate	$1e-4$	$1e-5$
batch size	256	32
num epochs	15	5
optimizer	AdamW ($\lambda = 0.01$)	AdamW ($\lambda = 0.01$)
loss	cosine similarity	cosine similarity

Table S1: Training hyperparameters for ALiBi-Dv2 in the low- and high-resolution training setups.

S2 Model details

S2.1 Hyperparameters

In Tab. S1 we list the hyperparameters used to train the ALiBi-Dv2 model, both for high- and low-resolution setup. Both configurations use the same optimizer and cosine similarity loss, while resolution, learning rate, batch size, and number of epochs differ.

S2.2 Trainable vs constant ALiBi heads

In Fig. S7, we compare training the ALiBi distance matrix scaling parameter m with keeping it fixed at a value of 1. Fixing the parameter results in qualitatively more homogeneous PCA compared to the model in which m is

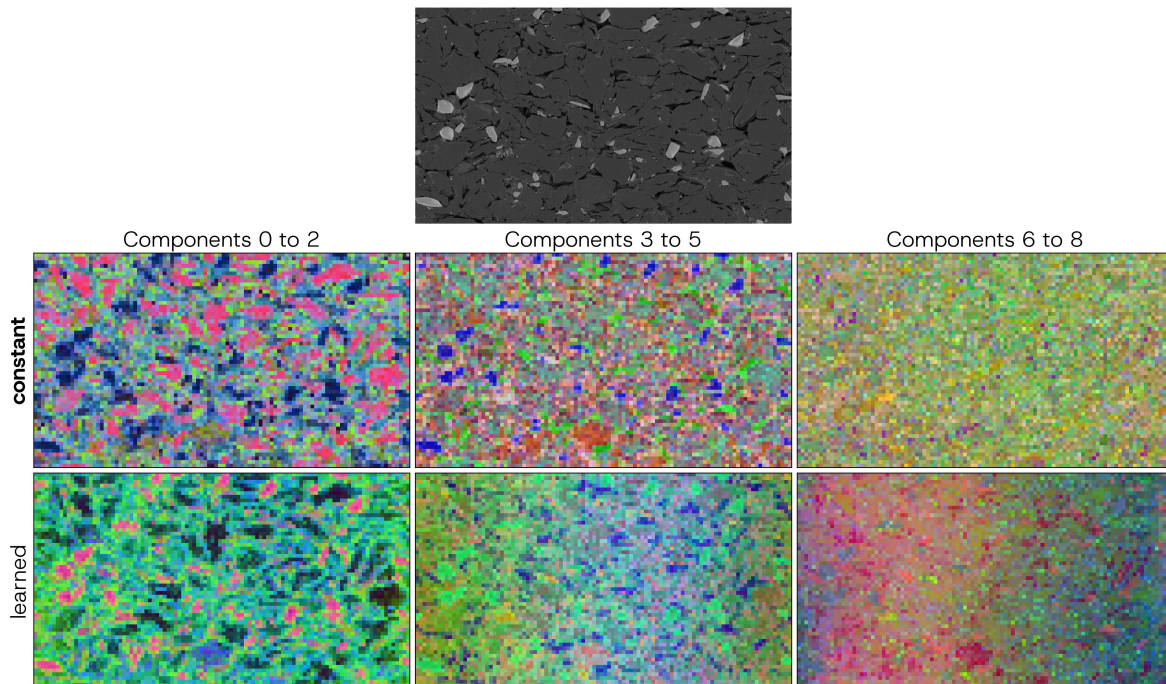


Figure S7: Comparing the impact of learned per-head ALiBi scalars m (bottom row) and constant $m 1$ (top row). We see learning the head scalars can lead to undesirable long-range positional biases.

learned during fine-tuning. We hypothesize that this arises because heads learn distinct length scales, thereby gaining the capacity to reconstruct positional biases across multiple layers.

S2.3 Multiscale training

We found training for a short period on larger images during finetuning results in better features for larger images (similar to [7, 8]). When images are simply resized to higher resolutions, the effective scale of visual features increases while the patch embedding continues to operate on fixed (14,14) pixel patches, leading to a mismatch in feature scales. This difference becomes particularly apparent in Fig. S8: models trained with a multiscale step clearly distinguish the cat’s head from its body, whereas models trained without multiscale augmentation fail to separate these regions. We see multiscale training also improves NoPE - this is further indication that multiscale training is largely about accommodating the patch-image feature size ratio, rather than for to adjust to new (interpolated) positional encoding values.

S3 NoPE vs ALiBi

The PCA visualizations in Fig. S9 demonstrate that ALiBi yields superior, more semantically meaningful feature representations compared to NoPE. By integrating explicit positional encodings, ALiBi successfully captures the spatial context of the image. Because NoPE lacks this spatial awareness, its resulting feature maps are less structured, struggling to separate distinct semantic regions and fitting more to texture and colour than semantics.

S4 Bias of the zero tensor

Of note in Fig. S5 is that there appears to be structure in the ALiBi-Dv2 features for an empty image. To further test this, we plot feature PCAs of low information images - namely the zeros tensor, a uniform grid of squares (of length patch size) and random noise - showing the results in Fig. S10. For the zeros tensor we see clear bar artefacts, and for the dot grid we see background inhomogeneities. For the random noise we see no structure.

We hypothesised this was due to compounding numerical imprecision (plus layer scales) in the model and our relative distance matrix. To test this, we add test-time jitter *i.e.* noise drawn $\mathcal{N}(0, \sigma_{\text{jitter}})$ to the distance matrix at each layer. As σ_{jitter} increases, the structure disappears.

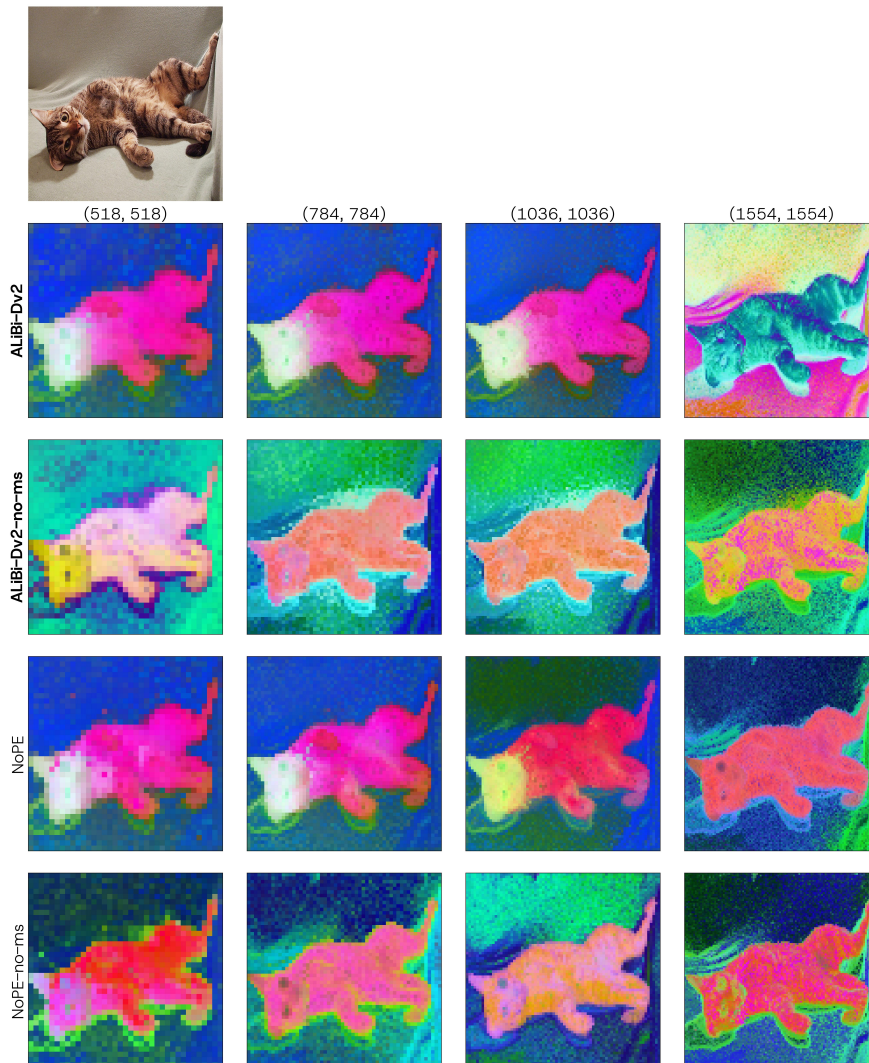


Figure S8: PCA visualizations of patch embeddings demonstrate that models trained with multiscale augmentation (ALiBi-Dv2, NoPE) successfully distinguish semantic regions (*e.g.* separating the head from the body) across varying input resolutions. Models lacking multiscale training (-no-ms) fail to separate these features, highlighting the necessity of multiscale training for adapting to varying feature scales.

We compare this to the feature PCAs for DINOv2, adding the noise to the input learned positional encoding (rather than ALiBi’s per-layer distance matrix). The structure persists more strongly than for ALiBi-Dv2. For DINOv2 there is structure for the random noise input.

S5 Input size extrapolation

Scaling to larger image resolutions highlights the varying generalization capabilities of the models. While DINOv2 and DINOv3 generalize well, our proposed ALiBi-Dv2 model’s features degrade at high resolutions. However, although it falls short of the highly robust scaling inherent to the DINO models, ALiBi-Dv2 still yields slightly more coherent and structurally meaningful representations compared to NoPE at these higher resolutions as seen in Fig. S11.

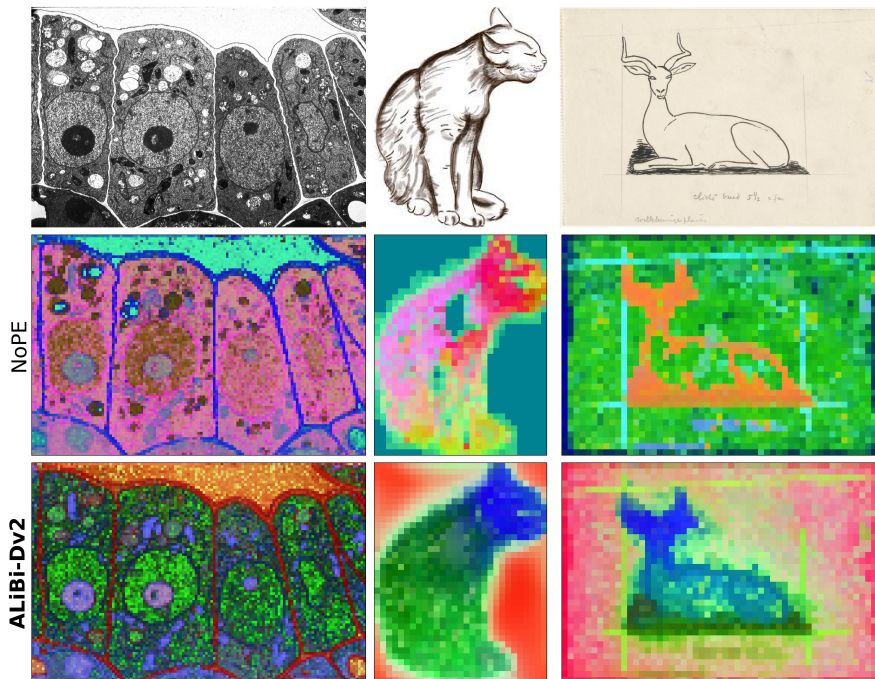


Figure S9: PCAs showing the shortcomings of not using positional encoding compared to ALiBi-Dv2.

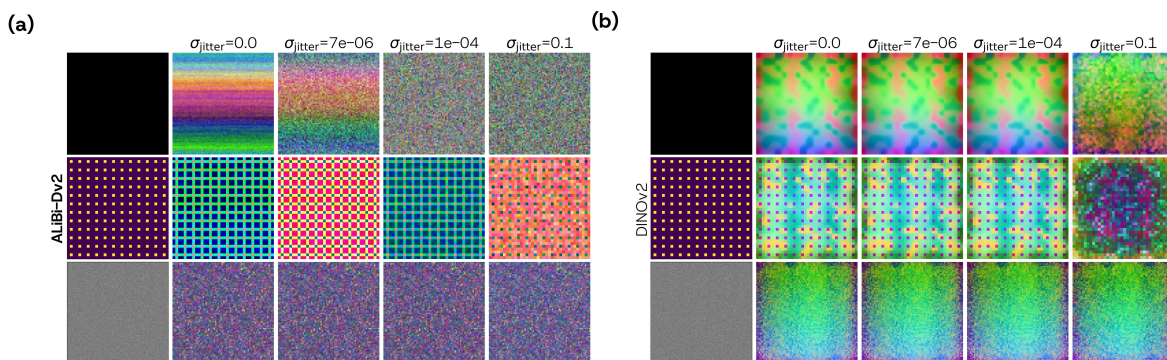


Figure S10: PCA of very low information images for (a) ALiBi-Dv2 and (b) DINOv2. with introduced random noise into the respective positional encodings.

S6 PCA visualisations

S6.1 Shared PCAs

Fig. S13 shows a shared PCA of foreground features for DINOv2 and our ALiBi-DV2. There is good agreement, regardless of position, size, orientation or number. This suggests the replacement of the learned PE has not damaged semantics.

S6.2 The perils of PCA visualisation

Fig. 5 and Fig. S12 show the same features for the same images from the same ViT backbones but with no feature scaling and with standard scaling (zero mean, unit standard deviation) before fitting the PCA. Scaling the features beforehand reduces how strongly the positional biases appear. This effect tends to be more apparent for out-of-distribution images (*i.e.* micrographs) - this is understandable, ViT features are naturally less expressive (lower variance and magnitude) for out-of-distribution data, and the positional biases then appear more strongly. It is worth noting that the ‘correct’ choice of feature scaling could hide these biases, which would still be present even if not shown.

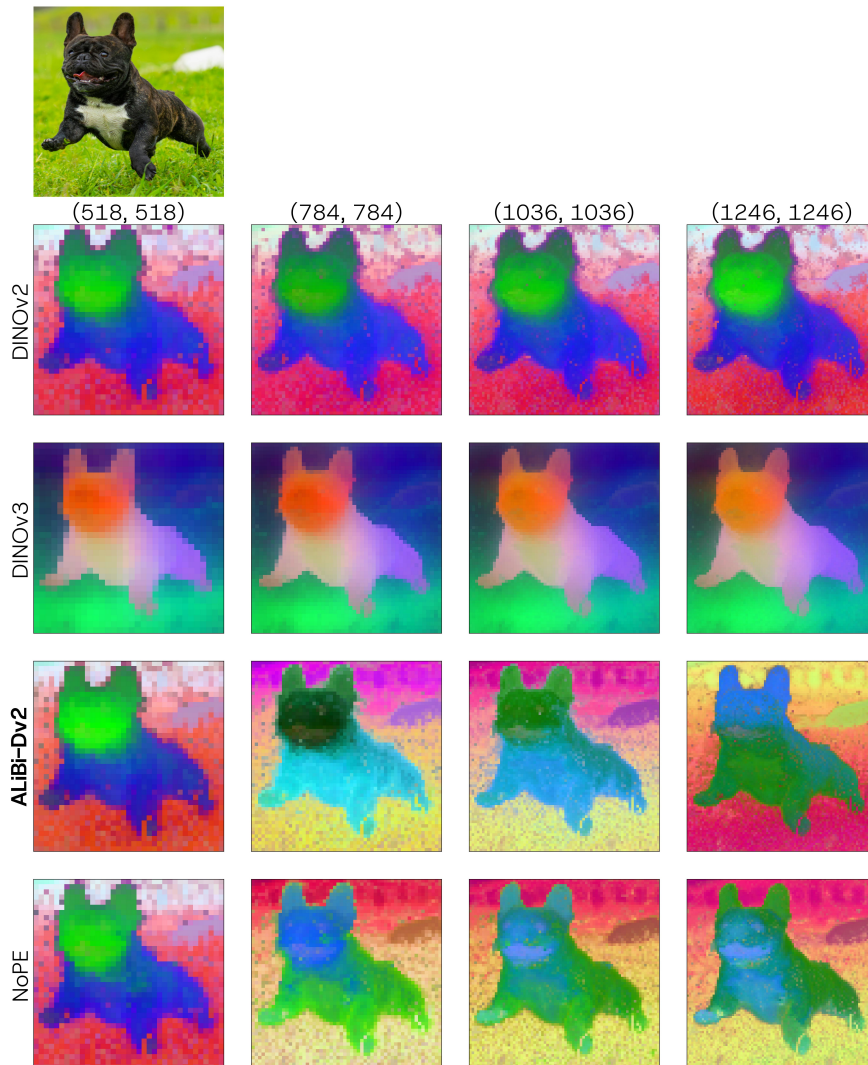


Figure S11: The grid shows PCA projections of patch features, organized by the evaluated model (rows) and the input image resolution (columns).

S7 Segmentation linear probes

S7.1 Training

The training procedure largely follows that of [7, 15]. We did not perform a grid search and instead fixed the learning rate at $1e-3$. Images were resized to (518,518) to match the patch size used in DINOv2. Since ADE20K contains substantially more classes than VOC12 or VOC07, the batch size had to be reduced. Due to computational constraints, the number of training epochs was lower than those reported in [7, 15]; however, we expect the general trends to remain consistent. For ADE20K, the 1k subsamples were randomly drawn from the full set of 20k training images in order to improve the logging of loss and mIoU during training.

S7.2 Transformation robustness

To quantify how robust the models and trained probes are to transformations, we perform the following experiment: transform an input image (flip-ud, roll, rot90), extract features from the ViT, apply the inverse transformation to the features and pass through the probe. Results are shown in Table S3. ALiBi-Dv2 is more robust to adversarial transformations, especially roll - thanks to wrap conditions in the ALiBi distance matrix it is effectively equivariant. DINOv2 is relatively robust to the roll transformation, which implies the linear probes were largely ignoring positional biases during training. We generally expect this to be the case - when fitting downstream

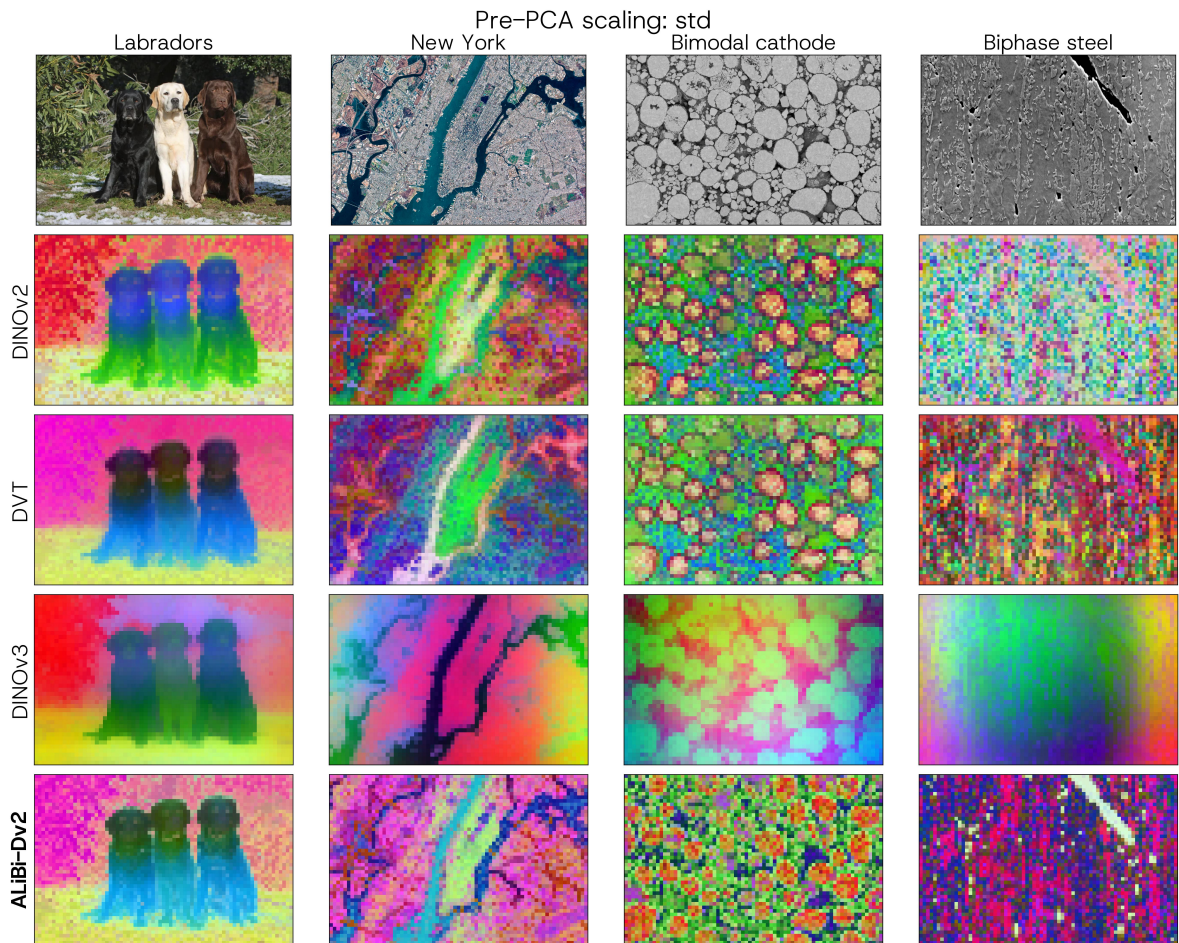


Figure S12: Feature PCAs with feature scaling before PCA. Although the positional biases are less strongly expressed in the visualisation, they are still present, and can still be fit to or clustered around during downstream tasks.

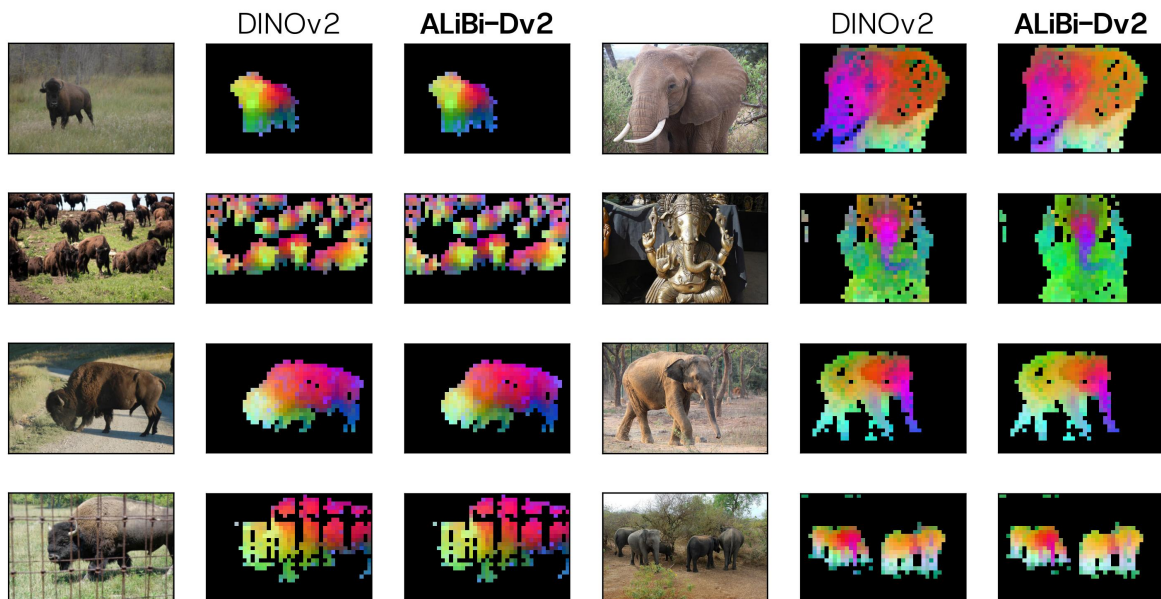


Figure S13: Shared feature PCAs for DINOv2 and ALiBi-Dv2. We see ALiBi-Dv2 retains DINOv2's feature similarities across changes in style, pose, *etc.*

	VOC07	VOC12	ADE20K
image size	(518, 518)	(518, 518)	(518, 518)
learning rate	1e-3	1e-3	1e-3
batch size	64	64	32
num epochs	75	50	50
samples per epoch	209	1,4k	1k
optimizer	AdamW($\lambda = 0.01$)	AdamW($\lambda = 0.01$)	AdamW($\lambda = 0.01$)
loss	cross entropy	cross entropy	cross entropy

Table S2: Training hyperparameters of the linear probe setup

Model	none	flip-ud	roll	rot90
DINOv2	0.762	0.4759	0.7601	0.456
NoPE	0.757	0.482	0.757	0.436
ALiBi-Dv2	0.769	0.499	0.769	0.445

Table S3: Validation mIoU for frozen-feature linear probe semantic segmentation of VOC12 as a function of image transform. ALiBi-Dv2 is generally more robust to transformations than DINOv2 or NoPE.

head networks to a large enough dataset these positional biases should be averaged away. The problem arises when applying these models in low- or no-data regimes, such as materials science.

S7.3 Linear probe predictions

Figure Fig. S14 provides additional qualitative examples of linear head predictions across the VOC07, VOC12, and ADE20K benchmarks. They are qualitatively all very similar due to the results shown in Tab. 3. But with minor improvements in VOC07 and VOC12 by ALiBi-Dv2 over DINOv2.

S8 Trainable segmentation

S8.1 Setup

We used the same classical features as Refs. [26, 27, 41], namely:

- A set of Gaussian blurs of the image with $\sigma \in \{0, 1, 2, 4, 8, 16\}$.
- Sobel filter and Hessian filter (plus eigenvalues) on each of these Gaussian blurred images.
- Difference of Gaussians across the blurs.
- Membrane projections (convolution with rotated line kernels) of the image.

We use an XGBoost classifier[62], and CRF post-processing [63].

S8.2 More examples

We present additional examples of trainable segmentation of battery materials in Fig. S15: a bimodal cathode (containing two different particle sizes for more efficient packing), a calendared (*i.e.* not compressed during manufacturing) cathode, a degraded cathode with cracking, and a cathode with the current collector included in the image. Again we see that positional biases express themselves, except in the case of our ALiBi-Dv2.

Note these are all nominally the same material: a Lithium-Nickel Manganese Cobalt oxide (NMC) cathode - a popular battery chemistry, especially for electric vehicles. Despite this the images vary quite considerably, due to manufacturing parameters or imaging choices. This wide variation in similar materials is what motivates low or no-training pipelines (such as trainable segmentation),

S8.3 Generalization & quantitative benchmarks

To quantify the improvement our ALiBi-Dv2 adds to materials trainable segmentation, we follow the experimental setup of Ref. [27]: training classifiers on a sparsely-labelled subset of an image-ground truth micrograph dataset (SEM images of nickel superalloys from [48]) and measuring mIoU across test images.



Figure S14: Visual comparison of linear head segmentation predictions using various backbones (DINOv2, NoPE, ALiBi) evaluated on the VOC07, VOC12, and ADE20K benchmarks

We replace their (dense) human labels with algorithmically generated scribbles, in order to measure the performance as a function of added labels. We train on 5 images and apply to a set of 17 unlabelled test images. Similar to Sec. 4.5 we use an XGBoost classifier and combine classical with ‘deep’ ViT features. Note we do not use a CRF. We apply labels in a ‘round’, where one round = one scribble label per-class per-training image (*i.e.* 3 classes \times 5 images = 15 labels per round). Labels are always correct, in that they respect the ground truth.

The results of this experiment are plotted in Fig. S16. Similar to Ref. [27], we find the addition of ViT features improves the mIoU drastically (around 0.3 points), as the classical features struggle with the variations in exposure and noise. ALiBi-Dv2 improves the mIoU compared to DINOv2 (best: 0.75 vs 0.69), especially at the start (0.57 vs 0.29) - we attribute this to the lack of positional bias. In a sparse, low-label regime where labels are randomly distributed across the image, it is possible for the classifier with DINOv2 to fit to spurious positional information (see Fig. 7 and Fig. S15) - this does not happen for ALiBi-Dv2.

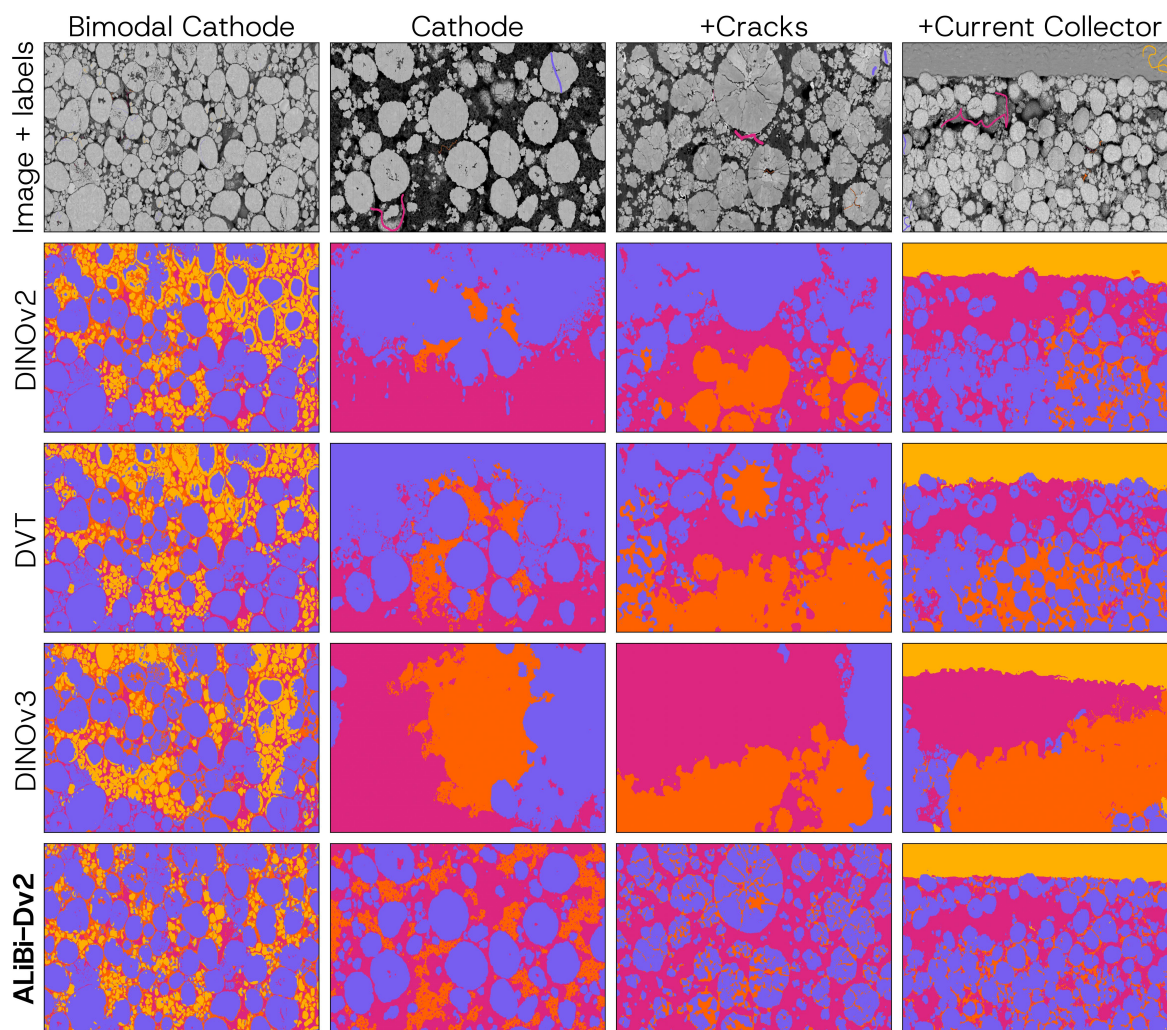


Figure S15: Further examples of trainable segmentation of battery materials using different ViT features. Data from Refs. [51], [47], [65] and [51], respectively.

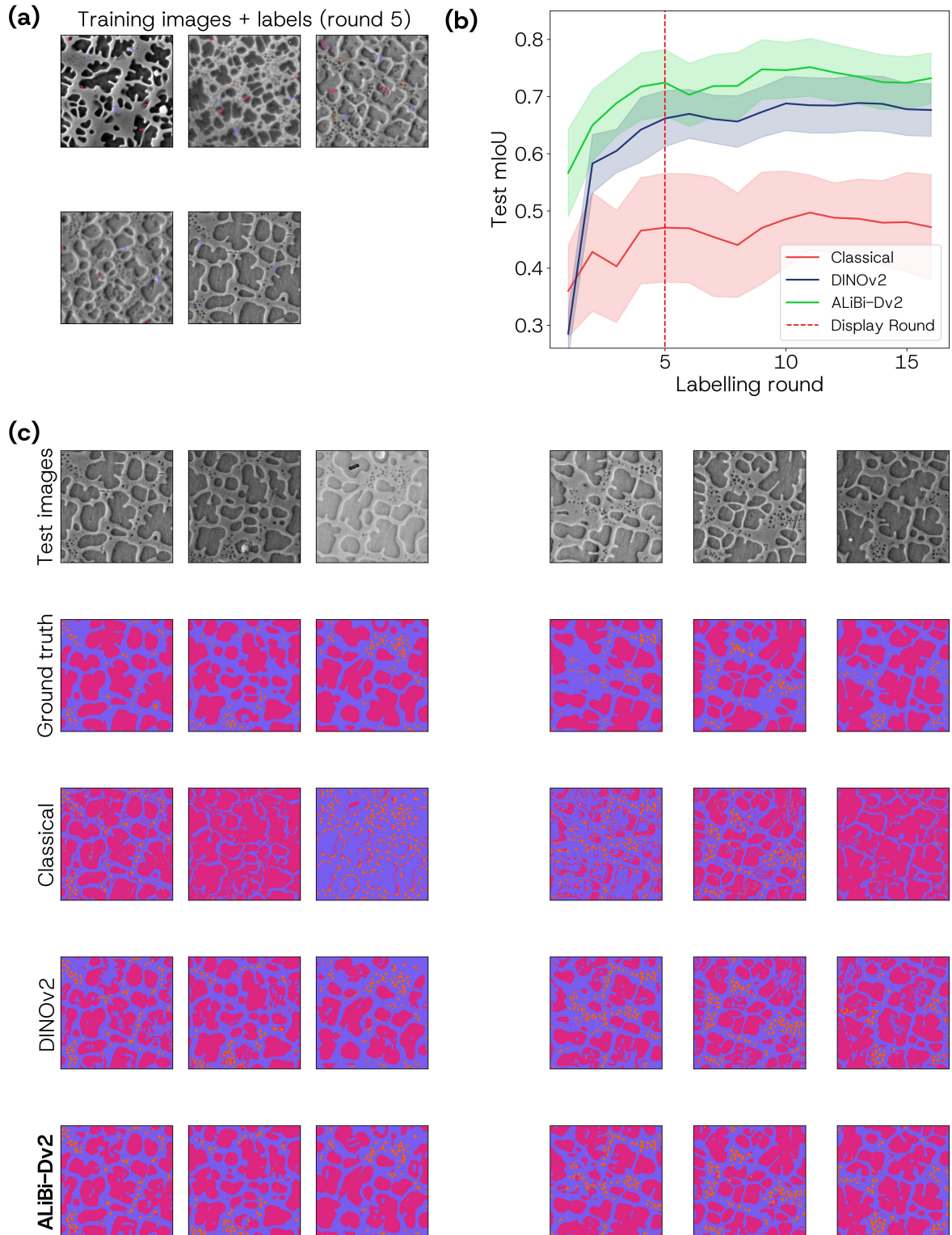


Figure S16: Trainable segmentation quantitative benchmark. **(a)** For a set of 5 training images, N rounds of human-like labels were added. **(b)** The class-averaged mIoU over 17 test images (with no labels) as a function of number of labelling rounds. **(c)** Example predictions of XGBoost classifier trained to map features \rightarrow labels after 5 labelling rounds for classical, classical + DINOv2 and classical + ALiBi-Dv2. ALiBi-Dv2 offers improved performance over DINOv2 with less labels due to the lack of positional bias in its features.